Transient Fluid Flow and Superheat Transport in Continuous Casting of Steel Slabs

B. ZHAO, B.G. THOMAS, S.P. VANKA, and R.J. O'MALLEY

The turbulent flow of molten steel and the superheat transport in the mold region of a continuous caster of thin steel slabs are investigated with transient large-eddy simulations and plant experiments. The predicted fluid velocities matched measurements taken from dye-injection experiments on full-scale water models of the process. The corresponding predicted temperatures matched measurements by thermocouples lowered into the molten steel during continuous casting. The classic double-roll flow pattern is confirmed for this 132 × 984 mm slab caster at a 1.52 m/min casting speed, with about 85 pct of the single-phase flow leaving the two side ports of the three-port nozzle. The temperature in the top portion of the molten pool dropped to about 30 pct of the superheat-temperature difference entering the mold of 58 °C. About 12 pct of the superheat is extracted at the narrow face, where the peak heat flux averages almost 750 kW/m^2 and the instantaneous peaks exceed 1500 kW/m^2. Two-thirds of the superheat is removed in the mold. The jets exiting the nozzle ports exhibit chaotic variations, producing temperature fluctuations in the upper liquid pool of ±4 °C and peak heat-flux variations of ±350 kW/m^2. Employing a static-*k* subgrid-scale (SGS) model into the three-dimensional (3-D) finite-volume code had little effect on the solution.

I. INTRODUCTION

CONTINUOUS casting of steel involves many complex phenomena including turbulent multiphase fluid flow, heat transfer, and solidification. The flow of molten steel and the associated transport of superheat in the upper portion of the liquid steel pool are critical to the quality of the final product. This flow starts downward from the bottom of the tundish and is driven by gravity through an submerged entry nozzle (SEN) at a rate controlled by a stopper-rod restriction near the nozzle top. The flow issues from two or more submerged ports near the bottom of the nozzle, which direct steel jets into the mold cavity. The jets traverse across the molten pool in the confined space contained within the solidifying steel shell. For a classic "double-roll" flow pattern, they then impinge obliquely onto the narrow face, causing a locally high heat-transfer rate to the shell. The impingement point often coincides with the exit of the mold, where the solidified shell must be thick enough to withstand the ferrostatic pressure to prevent molten steel from bursting through the shell, causing an expensive "breakout." Many casting operations restrict the casting speed according to the superheat in order to minimize the danger of such breakouts.

From the impingement point, the jets split upward and downward, flowing to create an "upper roll" above each jet and a "lower roll" in the lower regions of the strand. The exact nature of the flow pattern depends on the nozzle-port shape and angle, the submergence depth, the cast section size, the injected gas fraction, and the extent of electromagnetic stirring; these variables are studied elsewhere.[1–4]

B. ZHAO, Graduate Student, and B.G. THOMAS and S.P. VANKA, Professors, are with the Department of Mechanical and Industrial Engineering, University of Illinois at Urbana–Champaign, Urbana, IL 61801. Contact e-mail: bgthomas@uiuc.edu R.J. O'MALLEY, Plant Metallurgist, is with Nucor Steel Decatur LLC, Decatur, AL 35609.

Manuscript submitted May 23, 2005.

At the top surface, the molten steel should retain sufficient superheat and speed to avoid solidification of the meniscus, which can lead to subsurface "hook" formation and associated defects in the solidified product.[5] An insufficient superheat, thus, leads to increased surface defects. Finally, the superheat in the mold controls the internal microstructure and the associated macrosegregation of the final product. Specifically, the degree of superheat controls the formation and remelting of crystal nuclei that grow into the equiaxed grains that eventually comprise the center of the strand. These grains are beneficial for avoiding centerline segregation. Excessive superheat in the mold is, thus, associated with larger columnar grains and increased segregation and internal cracking problems. To avoid these defects, the liquid flow pattern and superheat must be carefully optimized.

Clearly, there is great incentive to quantify the turbulent heat transfer in the mold region of continuous casters. It is especially important to quantify the peak heat flux that causes thinning of the shell around the impingement region centered at the narrow face and the amount of superheat delivered to the shell during the critical early stages of solidification at the meniscus. Unfortunately, the harsh, high-temperature environment of the process makes direct measurement of the flow and temperature fields very difficult. Only a few measurements in the molten-steel caster have been attempted.[6,7,8] Transparent water models have provided most of the important insights into the transient flow features of the process,[7,9–12] but are severely limited in studying heat transfer. Thus, previous understanding of transient flow and heat transfer in the molten steel pool has relied mainly on computational models.[2,13]

This article first presents a large-eddy simulation (LES) model to predict flow and temperature in complex flows involving confined turbulent jets and validates it through comparison with relevant lab and plant measurements. It then presents results of this model applied to transient flow and heat transfer in the liquid pool of a typical continuous caster of thin steel slabs. These results are compared with

new measurements obtained by inserting thermocouples into an operating thin-slab caster.

II. PREVIOUS WORK

Only a few previous studies have simulated turbulent fluid flow and heat transfer within the liquid pool of a continuous casting machine. Thomas and Najjar[14] developed a two-dimensional finite-element model with the commercial code FIDAP using the two-equation k-ε turbulence model. Various solution strategies, relaxation factors, and meshes were investigated to help provide guidelines for achieving convergence. The predicted flow patterns and velocity fields showed reasonable agreement with measurements in a water model, and the predicted heat-flux profile was consistent with previous measurements. The results were sensitive to the choice of k and ε inlet conditions, wall laws, and turbulent Prandtl number. Huang, Thomas, and Najjar[13] used a three-dimensional (3-D), steady-state, k-ε model to simulate one-quarter of a mold, using the SIMPLE finite-volume solution method. The calculated temperatures in the molten steel agreed with one of the few published measurements, those by Offerman.[6] Over half of the superheat was shown to be removed in the mold, and the maximum heat input to the shell occurs near the jet impingement point on the narrow face. Furthermore, this heat input increases directly with superheat-temperature difference and casting speed.

Hasan and Seyedein[15,16] performed a 3-D finite-difference simulation on a staggered grid with a low-Reynolds-number k-ε model, including the liquid, mushy, and solid regions within a stainless steel caster. Different heat-extraction rates from the solid-surface boundaries were studied. Creech[4] evaluated various turbulence models in continuous-caster flow simulations, including the standard and low-Reynolds-number models, using the finite-difference package CFX.[17] Differences in peak heat flux up to 240 pct were found between different turbulence models, wall laws, and grid sizes near the shell. The low-Reynolds-number model, in particular, overpredicted the peak heat flux if the grid was too coarse. Thomas *et al.*[18] compared the best of these models with temperature measurements in a stainless steel thin-slab caster[19] and found reasonable agreement. A corresponding heat-transfer model of the solidifying shell and mold successfully matched the mold temperature, cooling-water heat-up, and shell thickness measurements.[18]

These previous models all employed popular Reynolds-averaged Navier–Stokes (RANS) methods to model the turbulence. The RANS methods decompose flow variables into mean and fluctuating components and feature separate transport equations for variables such as kinetic energy and dissipation, which are based on empirical constants. They also use special empirical boundary conditions called "wall laws." These methods are popular because they can be performed on coarse grids using few computational resources. They have proven successful for flow problems,[2,4,15] as documented previously.[3,8] However, the accuracy of the corresponding RANS heat-transfer models, with their associated wall laws, have received much less attention, especially in flowing metal systems. Furthermore, the RANS models are not well suited for the quantitative prediction of transient phenomena.

Other numerical methods exist to simulate turbulent fluid flow and the associated heat transfer. The most accurate method is direct numerical simulation (DNS), which resolves the details of turbulent flow by solving the Navier–Stokes equations on a very fine computational grid. Because the grid size needed to resolve all the turbulence scales increases with the 9/4th power of the Reynolds number,[20] fully turbulent processes such as continuous casting cannot be fully resolved using DNS even with the most powerful computers. The LES method involves an intermediate complexity between the DNS and RANS methods. In LES, the grid is fine enough to resolve the large scales of turbulence, while the small scales are assumed to be isotropic and are handled with a subgrid-scale (SGS) viscosity model. With better efficiency than DNS and a better fundamental basis than RANS, LES is used in the current work to simulate the complex flow and heat-transfer phenomena in continuous casting of steel.

Initial efforts to apply LES to fluid-flow phenomena in the continuous casting of steel have successfully matched particle-image velocimetry and other measurements including asymmetric fluid flow and transient particle motion.[8,21–23] Previous efforts have not considered transient heat transfer in the process, which is the subject of this work.

III. PLANT MEASUREMENTS

Measurements were conducted on the AK Steel thin-slab caster in Mansfield, OH, including flow in the mold using a water model and temperature in the liquid pool of the actual caster. The parallel mold of this caster is 132-mm thick × 984-mm wide × 1200-mm long and is described in detail elsewhere.[19] A stopper rod controls flow through the oval-bored SEN that features three exit ports: two rectangular side ports and a circular central port at the bottom. The nozzle is submerged 127 mm, measured from the molten-flux steel interface to the top of the side ports.

To study flow in the liquid pool, a full-scale water model was constructed,[19] including the tundish, the SEN with stopper-rod control, and a 2.6-m-long segment of the mold and strand with an automated level-control system. The water exiting from the mold bottom was recirculated back to the tundish, allowing time to establish pseudosteady-state conditions. The flow field was visualized by injecting dye into the SEN. Flow velocities were estimated through analysis of successive frames of videotape used to track movement of the dye front, knowing the time between frames.[22] The videotaped flow patterns can, thus, provide both qualitative and quantitative comparisons with the simulation results.

Measurements of the liquid steel in the mold are difficult, owing to the high-temperature environment of molten steel and the cramped space between the tundish and mold. The ability of computational models to quantitatively predict fluid velocities has been investigated previously with the help of velocity sensors in an operating steel caster.[8] For this work, an apparatus was constructed to measure vertical temperature profiles in the liquid steel pool in the mold, as pictured in Figure 1. The apparatus guides a thermocouple down through the top slag layer to a maximum insertion depth into the molten steel of 180 mm. The thermocouple consists of a double wire shrouded in a ceramic (alumina)

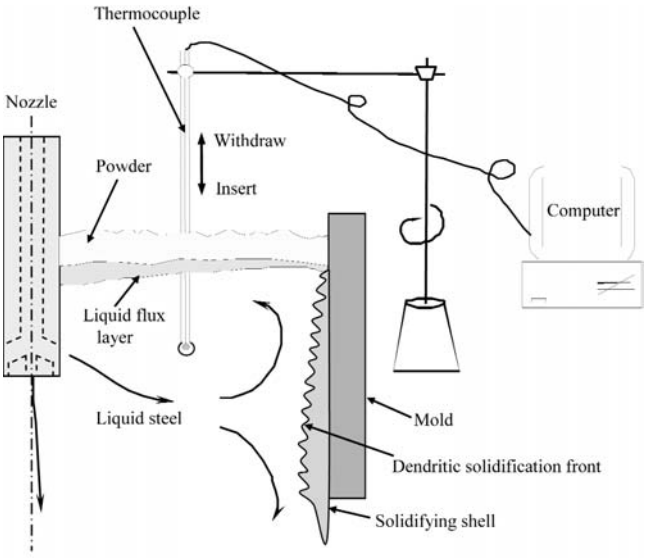

Fig. 1—Continuous-casting mold and apparatus to measure temperature in the liquid pool.

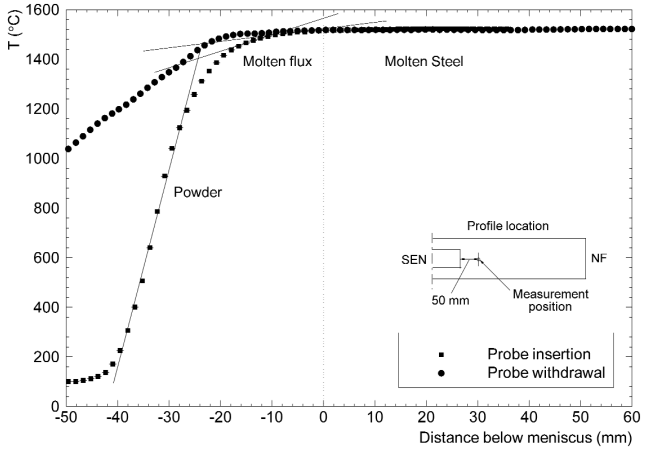

Fig. 2—Sample temperature measurement in the liquid pool.

rod about 15 mm in diameter. The thermocouple is moved down and up slowly (0.6 mm/s), allowing time for thermal equilibrium at the thermocouple tip. For each data set, temperatures were digitally recorded during both insertion and withdrawal.

An example of the temperature measurements is given in Figure 2. The temperature gradient decreases with increasing submergence depth, owing to the increasing thermal conductivity of the mold powder layer, liquid flux layer, and molten steel. The powder/flux and flux/steel interfaces are identified from the different slopes in these three regions. Table I gives the conditions for five different tests with a 129 mm nozzle-submergence depth, taken at different distances along the center plane between the wide faces. Two further tests were conducted with a 159 mm submergence depth, reported elsewhere.[24]

Table I. Experimental Conditions for Liquid-Steel Temperature Measurements in Caster

Number	Measurement Location	Casting Temperature	Powder Thickness (mm)	Flux Thickness (mm)
1	50 mm from SEN (150 mm from CL)	1558 °C	62	10
2	125 mm from SEN (225 mm from CL)	1558 °C	68	7
3	Midway from SEN to NF (295 mm from CL)	1559 °C	60	6
4	125 mm from NF (365 mm from CL)	1551 °C	68	5
5	50 mm from NF (440 mm from CL)	1558 °C	83	5

IV. COMPUTATIONAL MODEL

In this work, transient flow structures and the corresponding heat transfer are computed with 3-D LES in the liquid pool of the AK Mansfield thin-slab caster nozzle and mold. Figure 3 shows the simulation domain and coordinate system. It features the entire nozzle and one-half of the 1.2-m-long mold region, assuming symmetry about the centerplane. The computational grid consisted of 1.6 million cells, as shown in Figure 4. Although this grid captures most of the structures that control the flow, it does not resolve the very smallest eddies, so an SGS viscosity model is used. The grid is sufficiently fine that the subgrid model is not needed for stability; hence, a computation without the subgrid model is also performed for comparison.

A. *Governing Equations*

The following 3-D time-dependent Navier–Stokes and energy equations are solved numerically in a Cartesian coordinate system for the velocity, pressure, and temperature distributions.

Mass continuity:

$$\frac{\partial \bar{u}_i}{\partial x_i} = 0 \qquad [1]$$

Momentum:

$$\rho_0\left(\frac{\partial \bar{u}_i}{\partial t} + \frac{\partial(\bar{u}_i\bar{u}_j)}{\partial x_j}\right) = -\frac{\partial \bar{p}}{\partial x_j} + \frac{\partial}{\partial x_j}\left(\mu\frac{\partial \bar{u}_i}{\partial x_j}\right) + \frac{\partial Q_{ij}}{\partial x_j} + \delta_{i3}\rho_0\beta(\bar{T} - T_0)g \qquad [2]$$

Energy:

$$\frac{\partial \bar{T}}{\partial t} + \frac{\partial\left(\bar{u}_i\bar{T}\right)}{\partial x_i} = \frac{k}{\rho_0 C_P}\frac{\partial}{\partial x_i}\left(\frac{\partial \bar{T}}{\partial x_i}\right) + \frac{\partial Q_{Ti}}{\partial x_i} \qquad [3]$$

where $\bar{u}_i$ represents "grid-filtered" velocities in the x, y, and z directions (represented by $i, j = 1, 2, 3$), $\bar{p}$ is the pressure, $\bar{T}$ is the temperature, μ is the dynamic viscosity, ρ_0 is the density at the reference temperature (T_0), β is thermal-expansion coefficient, g is the gravitational acceleration, k is the thermal conductivity, C_p is the heat capacity, and δ_{i3} is the Kronecker

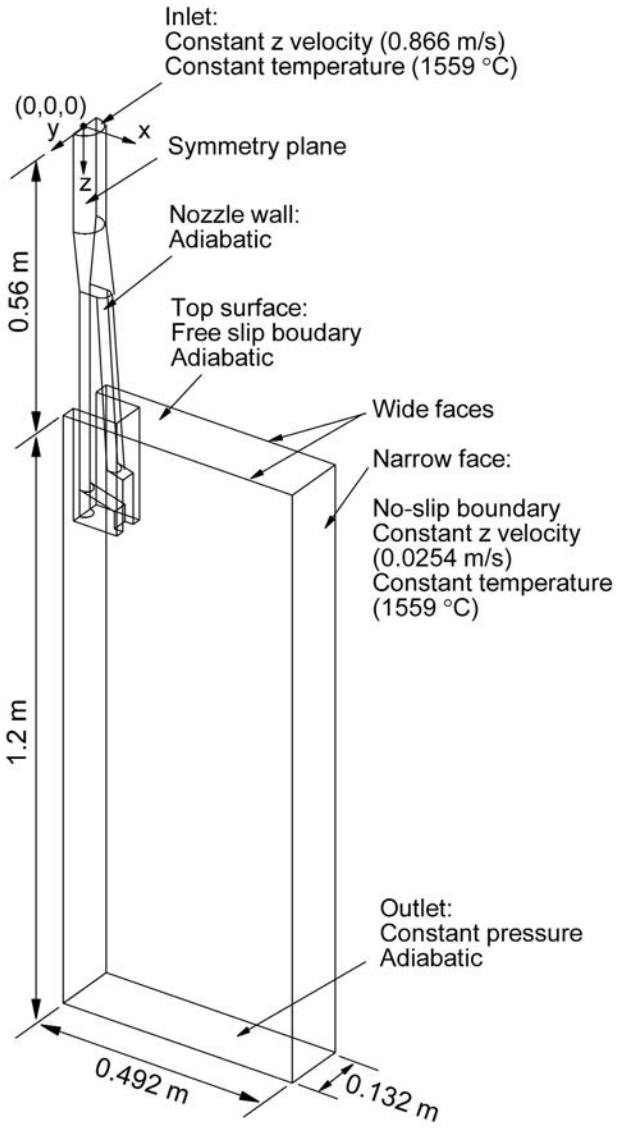

Fig. 3—Caster simulation domain and boundary conditions.

delta (equal to 1 if $I = 3$; otherwise, equal to 0). The momentum equations and the energy equation are coupled through a buoyancy term in the z momentum equation, using the Boussinesq approximation.[25]

The term Q_{ij} represents the subgrid momentum fluxes and can be expressed as

$$Q_{ij} = \rho_0(\overline{u_i u_j} - \overline{u}_i \overline{u}_j) \quad [4]$$

The trace of Q_{ij} is included into the pressure, and the trace-free part of Q_{ij} (labeled τ_{ij}) is modeled in terms of the resolved scales. A model based on eddy viscosity is used, in which τ_{ij} is assumed to be proportional to the symmetric strain-rate tensor of the resolved scales. The proportionality constant (μ_T) is defined by

$$\tau_{ij} = Q_{ij} - \frac{1}{3} Q_{kk} = 2\mu_T \overline{S}_{ij} \quad [5]$$

$$\overline{S}_{ij} = \frac{1}{2}\left(\frac{\partial \overline{u}_i}{\partial x_j} + \frac{\partial \overline{u}_j}{\partial x_i}\right) \quad [6]$$

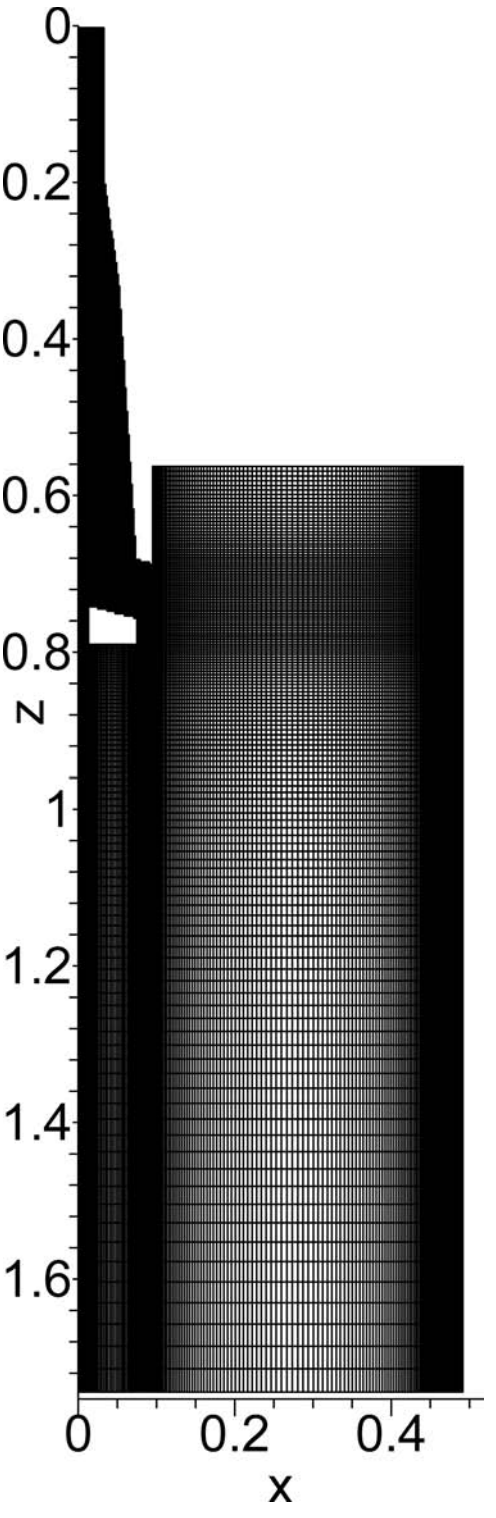

Fig. 4—Model domain and grid detail.

Combining Eqs. [4] through [6] gives the following expression for the subgrid flux term in Eq. [2]:

$$\frac{\partial Q_{ij}}{\partial x_j} = \frac{\partial}{\partial x_j}\left(\mu_T \frac{\partial \overline{u}_i}{\partial x_j}\right) + \frac{\partial}{\partial x_j}\left(\mu_T \frac{\partial \overline{u}_j}{\partial x_i}\right) \quad [7]$$

The turbulent-eddy viscosity is calculated here from the following subgrid-velocity-scale equation:[26]

$$\mu_T = C_v \rho_0 K_G^{1/2} \Delta \quad [8]$$

where the constant C_v is 0.05, and Δ is the grid-length scale, given by $\Delta = (\Delta_x \Delta_y \Delta_z)^{1/3}$ (Δ_x, Δ_y, and Δ_z are grid sizes in the x, y, and z directions, respectively). The kinetic energy, $K_G = \overline{u_i' u_i'}/2$, is determined by solving a transport equation given by[26]

$$\rho_0 \left(\frac{\partial K_G}{\partial t} + \overline{u}_j \frac{\partial K_G}{\partial x_j} \right) = \frac{1}{2} \mu_T \left(\frac{\partial \overline{u}_i}{\partial x_j} + \frac{\partial \overline{u}_j}{\partial x_i} \right)^2 - \rho_0 C_\varepsilon \frac{K_G^{3/2}}{\Delta} + \frac{\partial}{\partial x_j} \left[\left(\mu + \rho_0 C_{kk} K_G^{1/2} \Delta \right) \frac{\partial K_G}{\partial x_j} \right] \quad [9]$$

where the constant C_ε is 1.0 and C_{kk} is 0.1.

The term Q_{Ti}, representing the SGS heat fluxes,

$$Q_{Ti} = \overline{T}\,\overline{u}_i - \overline{T u_i} \quad [10]$$

is modeled as an extra diffusion term using the eddy-viscosity value μ_T from the momentum equation and the turbulent Prandtl number (Pr_T):

$$\frac{\partial Q_{Ti}}{\partial x_i} = \frac{\mu_T}{\mathrm{Pr}_T} \frac{\partial}{\partial x_i} \frac{\partial \overline{T}}{\partial x_i} \quad [11]$$

where Pr_T is 0.9.

B. *Boundary and Initial Conditions*

The boundary conditions are summarized in the simulation domain in Figure 3, which contains one-half of the liquid pool of the continuous caster. The left-hand wall represents the symmetry plane between narrow faces, where the normal velocity component and the gradients of other variables are, thus, set to zero. The asymmetries ignored by this assumption are investigated elsewhere.[22,23]

The wide- and narrow-face domain boundaries represent the dendritic solidification front of the inside of the solidifiying steel shell. In a real caster, the solidifying shell grows in thickness with distance below the meniscus. However, for the domain length simulated, the maximum shell thickness is less than 4 pct of the domain width. Thus, the wide and narrow faces were assumed to be straight walls with no-slip boundary conditions, with the axial (z) velocity component set to the casting speed, to match the withdrawal rate of the shell. Neglect of the shell-thickness effect, which is also intrinsic to water models, slightly exaggerates flow variations through the domain thickness, as investigated elsewhere.[22] However, the effect on jet impingement along the narrow face, which is of primary concern in this work, is minor. For thermal boundary conditions, these walls are set to a constant temperature equal to the liquidus solidification temperature of the steel alloy.

Level fluctuations of the top free surface are around 5 mm.[22] This minor shape change was assumed to have negligible effect on the flow, so the top surface was modeled as a rigid plane with zero normal velocity and zero gradients prescribed for other variables. An adiabatic thermal boundary condition is prescribed over the top surface, because previous work has shown that heat loss through the insulating flux and powder layers is small.[27] The domain outlet is artificially cut off at a horizontal plane 1.2 m below the meniscus, where a constant pressure is prescribed. Heat leaves the domain outlet only through advection.

Flow through the nozzle is not the main concern of this study, so the inlet condition to the nozzle is a uniform velocity corresponding to the flow rate and measured casting speed. Nonuniformities from a properly centered stopper-rod flow control are expected to be small. The nozzle is long enough for the flow to become fully turbulent before entering the mold. The nozzle inlet temperature is set to a constant "casting temperature" measured in the tundish. The nozzle walls are assumed to be adiabatic, as the alumina-graphite is a good insulator and the residence time is very short.

In transient simulation of a pseudosteady-flow field, the initial conditions do not affect the accuracy of the final solution, but will influence the integration time needed to reach a statistically stationary state. Zero flow velocities and the liquidus solidification temperature of the steel are assumed initially throughout the domain.

C. *Computational Details*

Equations [1] through [3] are solved using a finite-volume approach described in Appendix I and elsewhere.[22] Table II lists the parameters and properties of the liquid steel used in the simulation. The dimensions and operating conditions are chosen to match the conditions of the experiments conducted on the real steel caster. The thermal-expansion coefficient, 10^{-4} °C^{-1}, is based on liquid-density measurements.[28] For the small temperature difference in the present problem (57 °C), the Boussinesq approximation is valid.

A computational grid consisting of 1.64 million cells was used. Curved surfaces are modeled using a stair-step grid.

Table II. Parameters and Material Properties for Steel Caster Simulation

Mold (domain) thickness	132 mm
Mold (domain) width	492 mm
Nozzle domain length (to port top)	687 mm
Strand domain length	1.2 m
Model domain length (total)	1.76 m
Nozzle bore diameter	70 mm
Side nozzle port height	75 mm
Side nozzle port width	32 mm
Bottom nozzle port diameter	32 mm
SEN submergence depth	127 mm
Casting speed	25.4 mm·s^{-1}
Casting temperature (nozzle inlet)	1559 °C
Steel grade	434 stainless
Steel liquidus temperature	1502 °C
Reference temperature (T_0)	1502 °C
Laminar viscosity	0.00555 kg·m^{-1}·s^{-1}
Thermal conductivity	26 W·m^{-1}·°C^{-1}
Density	7020 kg·m^{-3}
Specific heat	680 J·kg^{-1}·°C^{-1}
Thermal-expansion coefficient	1.0×10^{-4} °C^{-1}
Gravity acceleration	9.8
Reynolds number (at side ports)	56000
Laminar Prandtl number	0.1452
Turbulent Prandtl number	0.9

The maximum velocity and temperature gradients occur near the nozzle ports, the jet-shear layer, and near the solidifying shell. Hence, the grid was stretched in all directions using a ratio below 1.03 to optimize the grid refinement, achieving cell spacings ranging from 2 mm at the port, and 0.7 mm near the solidifying shell, to a maximum of 20 mm in the central regions, where the gradients are small.

The FORTRAN computer program UIFLOW, developed in the Computational Fluid-Dynamics (CFD) lab at the University of Illinois at Urbana Champaign, was used for the computation. A time-step $\Delta t = 0.0005$ s, satisfying the Courant–Friedrichs–Lewy[20] stability condition for the convective terms and diffusion-time-step, was used. The computations were performed on 1.7 GHz personal computers with 2 GB memory in the CFD lab, requiring ~32 central processing unit seconds per time-step. Snapshots of the results were saved every 100 time-steps (0.05 seconds) to make animations.

V. MODEL VALIDATION

The ability of the UIFLOW code to accurately simulate velocity has been validated extensively in previous work.[22] To investigate the accuracy of this LES code for computing turbulent heat transfer, it was applied to a relevant test problem, where careful measurements were available for comparison. The problem is an axisymmetric air jet impinging on a cooled flat copper surface, as pictured in Figure 5. Heat flux to the wall was measured as a function of radial distance. Spatial variables are characterized by the inlet-nozzle diameter (D), given in Table III, together with the nozzle height above the plate, the air properties, and temperature conditions. Although the real jet is unbounded in the radial direction, the 3-D model domain was 160 mm in diameter, with an exit slit 10-mm high. The inlet-nozzle domain was assumed to be an ~10-D-long tube that was perfectly aligned. The complete computational grid had 822,400 cells. The scaled velocities in this problem are similar to those in the continuous casting process, with a Reynolds number in the nozzle of about 20,000 and a nozzle distance from the impingement surface of about 5 inlet diameters.

The computed time-averaged flow pattern is given by the velocity vectors in Figure 6(a) and features three distinct regions: the vertical "free jet" just below nozzle exit, the "stagnation region" near the impingement point, and the horizontal "wall-jet" region. Figure 6(b) shows the corresponding time-averaged temperature contours, and Figure 7 gives the heat-flux profile along the wall. In the free-jet region, the jet entrains surrounding fluid, causing it to spread and slow down slightly. Very near the stagnation point, the heat flux reaches its maximum. The impinging jet then turns 90 deg into a strong radial flow that creates an expanding boundary layer in the wall-jet region. The heat flux continually decreases with radial distance. In the model, an artificial increase in heat flux is generated near the outlet slit. Otherwise, the simulation

Table III. Axisymmetric-Jet Problem Conditions

Inlet diameter (D)	10 mm
Nozzle-to-plate distance (H)	50 mm
Inlet temperature (T_p)	25 °C
Ambient temperature (T_a)	25 °C
Plate-surface temperature (T_s)	8 °C
Density of air (ρ)	1.2 kg·m^{-3}
Molecular viscosity (μ)	17.85 × 10^{-6} Pa·s
Thermal conductivity (k)	0.025 W·m^{-1}·°C^{-1}
Specific heat (C_p)	1006 J·kg^{-1}·°C^{-1}
Prandtl number (Pr)	0.71
Reynolds number (Re)	20,000
Inlet bulk velocity (V_b)	29.75 m·s^{-1}
Time-step (Δt)	5 × 10^{-7} s

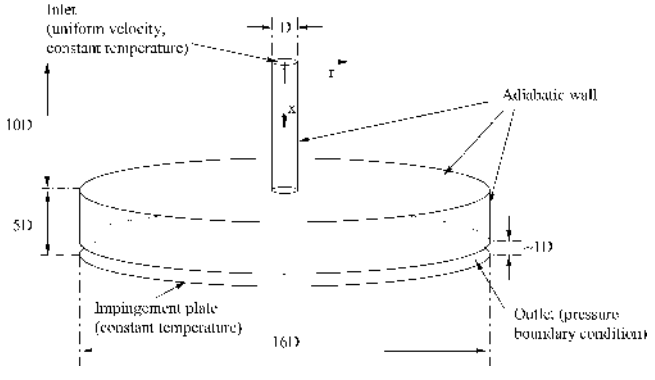

Fig. 5—Air-jet impingement-validation-problem domain and boundary conditions.

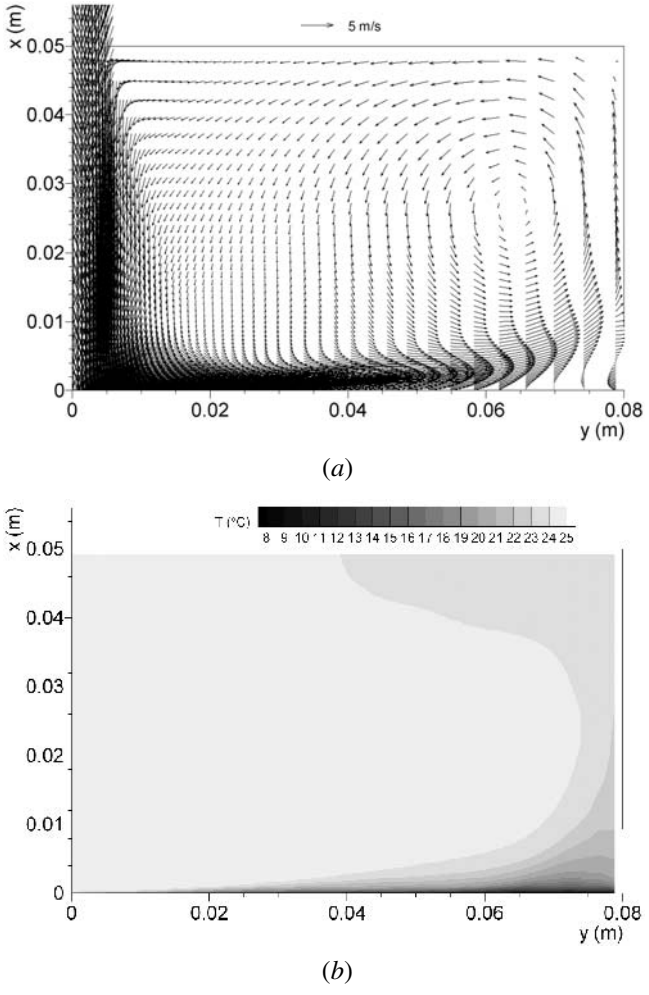

Fig. 6—Air-jet problem (*a*) computed mean velocity field and (*b*) corresponding mean temperature field.

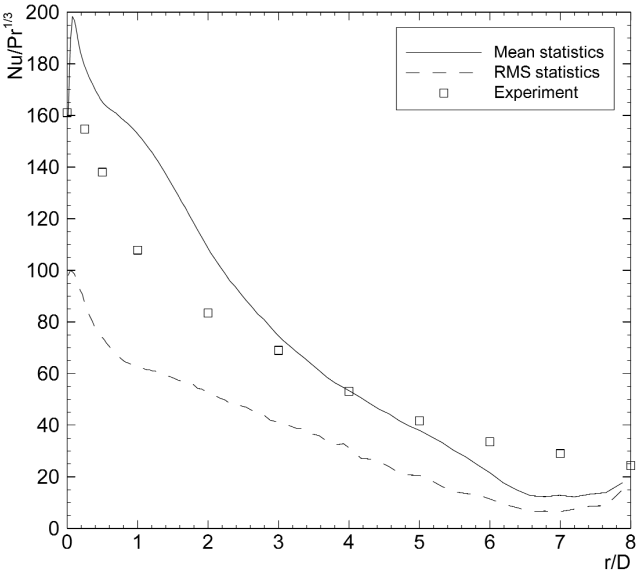

Fig. 7—Comparison of computed and measured mean heat-flux profile in the air-jet problem.

heat-flux profile closely matches the measurements. The computed velocities also are consistent with measurements, as reported elsewhere.[29] This agreement suggests that the model and grid refinement employed in this work should produce reasonable results for the continuous-casting problem.

VI. RESULTS AND DISCUSSION

The discretized Navier–Stokes and energy equations were integrated in time to reach a statistically stationary state of the flow and temperature fields in the liquid pool of the continuous-casting mold domain. First, over 15 seconds were computed with stationary wall conditions and without buoyancy. Next, a further 15 seconds were simulated with the downward velocities along the wide- and narrow-face walls fixed to the casting speed. Then, buoyancy forces were activated for the remainder of the simulation. No significant changes in either flow pattern or temperature field were observed. This suggests that both the drag effect of the shell and natural convection are unimportant, which agrees with previous work.[13,22] After several more flow seconds, mean flow statistics were compiled for 40 seconds, and, during the latter 20 seconds of this, root-mean-square (RMS) values[22] were calculated to reveal the average magnitude of the velocity and temperature fluctuations. Finally, the SGS model was turned on, and results and mean statistics were again gathered for a further 40 seconds, with RMS statistics computed during the latter 20 seconds. The results with and without the SGS model are similar. Thus, the following sections present the results with the SGS model, except when the two models are compared.

A. *Mean-Velocity Field*

The mean-velocity fields in the *x-z* center plane of the nozzle and mold are shown in Figure 8, averaging instantaneous velocities for 40 seconds. The velocity fields and corresponding streamlines are shown for other planes in Figures 9 through 12. Most of the flow enters the mold as strong jets from the bottom portion of each side port, as shown in Figure 8(b). There is also a strong swirl component to the flow, which makes the flow extend to the top corners of the side port. A slow recirculation in the top-central region of the side port causes flow to intermittently reenter the nozzle. This is due to the oversized area of the ports relative to the nozzle bore.[30,31,32] The side jet leaves the nozzle at an average downward angle of 26 deg relative to the horizontal. A notch is missing from the bottom of the side port in this design, but this appears to have relatively little effect on the flow, as velocity in the notched region is very low. Only 15.4 pct of the flow is computed to exit through the small third port located at the center of the nozzle bottom.

Each side jet expands as it entrains fluid while traversing across the liquid pool. The jet impinges on the narrow face and splits into upward and downward wall jets. The impingement point is 0.365 m below the top surface (0.925 m in Figures 8 and 13). This point lies 8 mm above the intersection point with the 26-deg axis of the initial jet, which indicates the slight upward curvature experienced by the jet as it crosses the mold. From the impingement point, the flow spreads in all directions, as shown in the *y-z* cross section through the flow field near the narrow face, shown in Figure 10.

The upper wall jet lifts the meniscus at the narrow face and then turns back across the top surface toward the SEN. This forms a large recirculation region above the jet that is referred to as the "upper roll" (Figure 8). The center or "eye" of the upper roll is located 0.15 m below the top surface and 0.172 m to the left-hand side of the narrow face. A large portion of the jet goes down toward the outlet of the domain and eventually forms a very large recirculation region below the jet. This recirculation region is often referred to as the "lower roll." The eye of this lower roll is located 0.56 m below the top surface and 0.15 m to the left-hand side of the narrow face.

Downward flow out of the center port acts much like a free jet, except it is bounded by the two wide faces. In the *y-z* plane, this central jet spreads quickly, touching the wide faces about 0.1 m below the port exit, as shown in Figure 9. In the *x-z* plane, the central jet interacts with the lower roll to create a third recirculation region. This is demonstrated more clearly in the streamline plot in Figure 13.

An interesting and important feature of the mean flow field (Figure 8) is the presence of a small but persistent vortex at the top-right corner of the domain, which comprises the narrow-face meniscus. This vortex forms as the upward wall jet moves against the downward-dragging shell. This vortex is important to heat transfer, as discussed in the next section.

Figures 11 and 12 show mean flow fields in two cross sections parallel to the top surface. Near the top surface, Figure 11 shows the strong uniform flow toward the SEN that is characteristic of this classic double-roll flow pattern. As this flow passes the SEN, there is flow separation at the corner of the SEN and vortices are generated. These persistent vortices are detrimental, as they encourage erosion of the SEN refractory, with consequent local contamination of the mold flux, meniscus infiltration problems, and centerline surface defects.

Figure 12 shows a cross section that cuts through the wall jet in the lower recirculation zone, revealing many vortices. The vortices near the narrow-face corners are generated at the impingement point when the spreading flow in Figure 10 is turned back along the wide faces. The resulting swirls produce a long vertical spiral motion, which appears on the cross section as symmetric swirls. This same helix structure can be observed in the wall jet going up along the narrow face and in

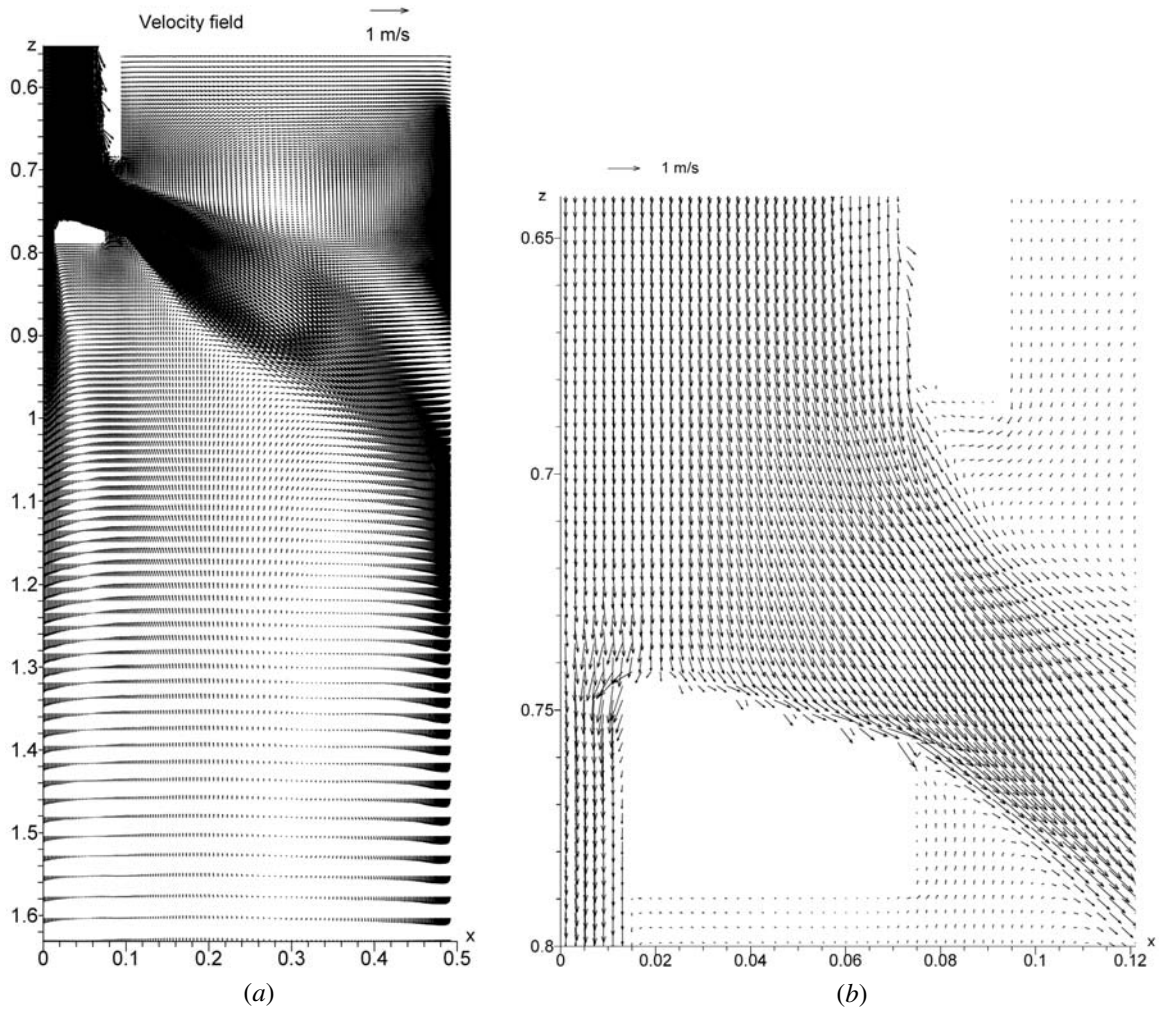

Fig. 8—Mean-velocity field in the caster *x-z* center plane, showing (*a*) the overall mold region and (*b*) detail within the nozzle.

water models of the process. Near the central downward jet, further vortices are generated, indicating a helix structure and wobbling of the center jet. The asymmetric nature of these vortices in Figure 12 reveals this transient nature and shows that the time scale of the phenomenon is longer than the 40-second averaging period. This natural vortex-shedding phenomenon is complicated by its confinement within the wide-face walls and interactions with the flow in the lower recirculation-zone flow.

B. *Flow-Model Validation*

The flow pattern predicted in both the nozzle and mold regions is similar to recent uncoupled simulations of the entire nozzle and mold.[22] To further evaluate the accuracy of the model, the predictions were compared with measurements in a water model. The computed streamlines are superimposed onto a photograph of dye injection into the water model in Figure 13. The simulated flow pattern matches very well with the experiments.

Experimental velocities were found by tracking the movement of the dye front in successive frames of a video recording.[22] In Figure 14(a), the velocity along the jet axis is compared with the measured velocities. This measurement has uncertainties, as the dye front must be approximated through the thickness of the water model, and dye diffusion is ignored. However, the predictions match the measurements quite well.

In Figure 14(b), the horizontal velocity profiles across the top surface are compared. Although the qualitative shape is similar, the model underpredicts the dye-injection measurements. It also underpredicts the previous simulation results.[22] This suggests that surface velocities are very sensitive to minor changes in the flow pattern and can persist at levels quite different from the mean for time periods exceeding 40 seconds. Overall, the model is judged to be reasonably able to predict the flow field in continuous casting.

C. *Mean-Temperature Field*

The temperature in the molten-steel pool is controlled by the flow pattern. It varies by 57 °C between the casting temperature entering the nozzle from the tundish bottom and the liquidus solidification temperature of the steel (Table II). The temperature difference above the liquidus represents a measure of the "superheat" contained in the molten steel.

The mean-temperature field computed in the center plane is shown in Figure 15. Heat loss from the nozzle is negligible, so the jets enter the mold region at roughly the casting

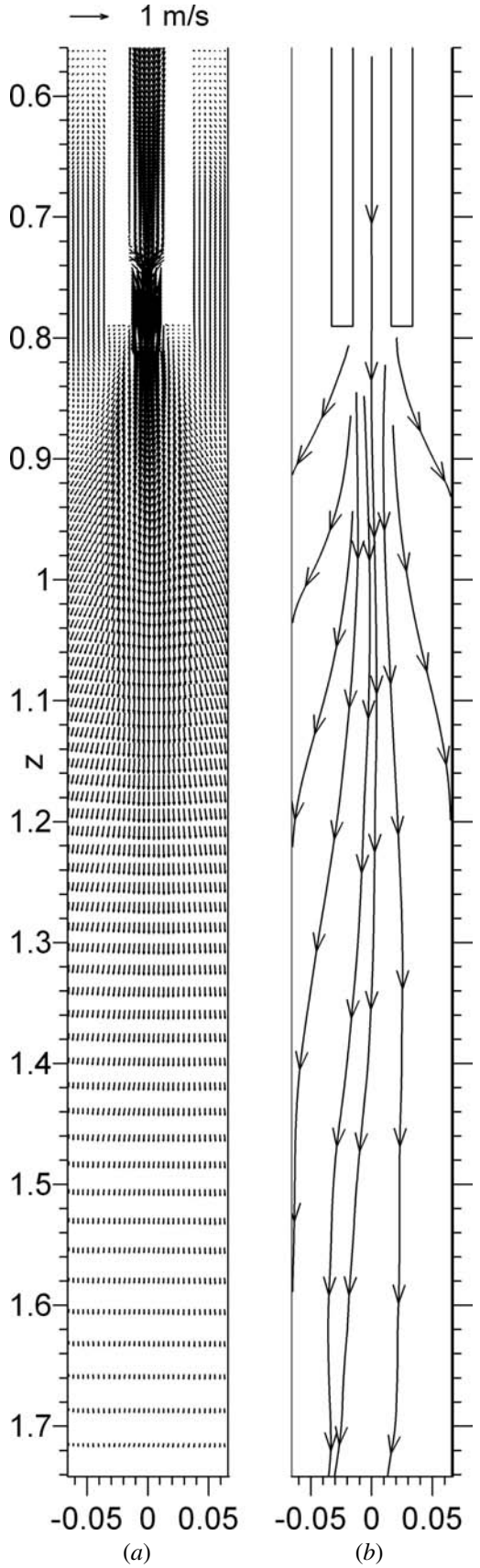

Fig. 9—Mean-velocity field in caster *y-z* center plane, showing (*a*) the central jet exiting the nozzle bottom through third port and (*b*) the corresponding streamlines.

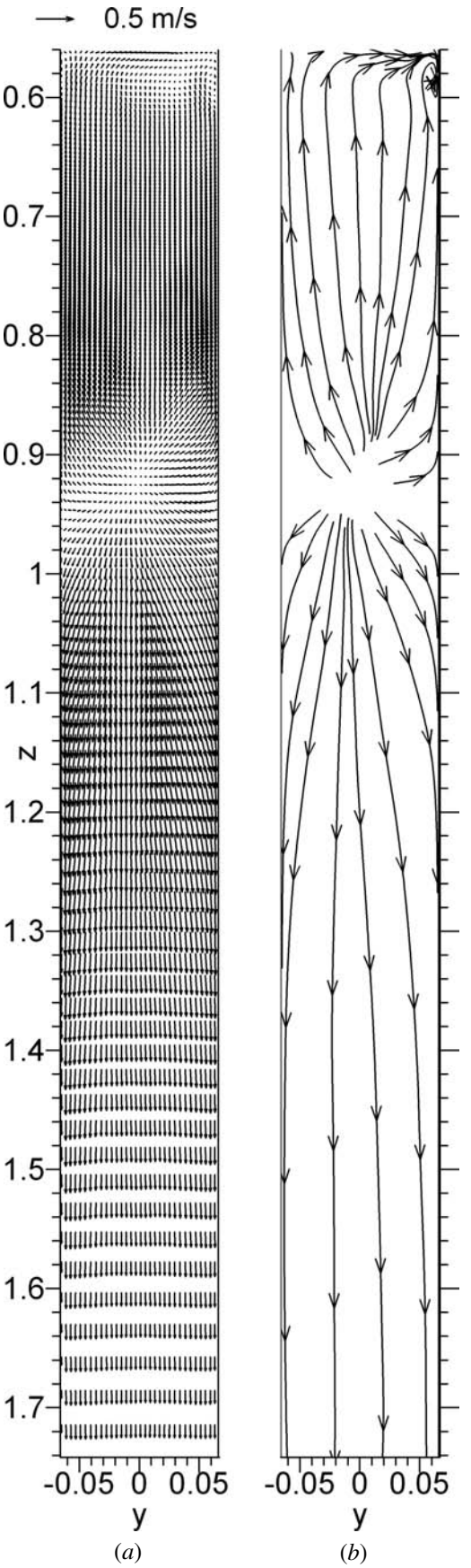

Fig. 10—Mean-velocity field in the *y-z* plane 17 mm from the narrow face, showing jet impingement on (*a*) the narrow face and (*b*) the corresponding streamlines.

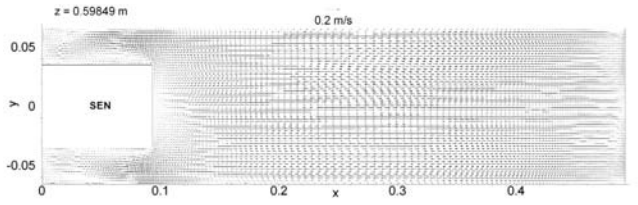

(*a*)

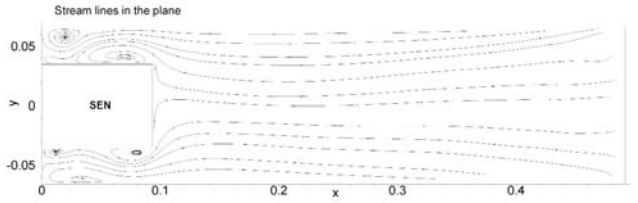

(*b*)

Fig. 11—Mean-velocity field in the *x-y* plane 38.5 mm below the top surface, showing (*a*) the mean flow toward the SEN and (*b*) the corresponding streamlines that show vortexing near the SEN.

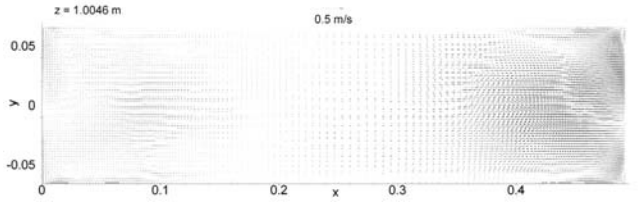

(*a*)

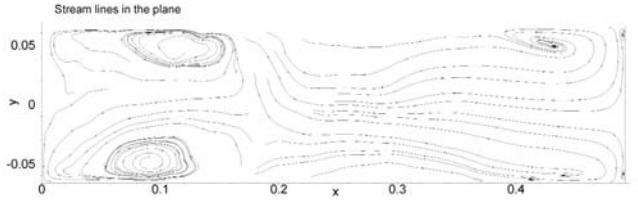

(*b*)

Fig. 12—Mean-velocity field in the *x-y* plane 445 mm below the top surface (*a*) cutting through the side jet in the lower recirculation zone and (*b*) corresponding streamlines that show vortexing near corners of the wall jet.

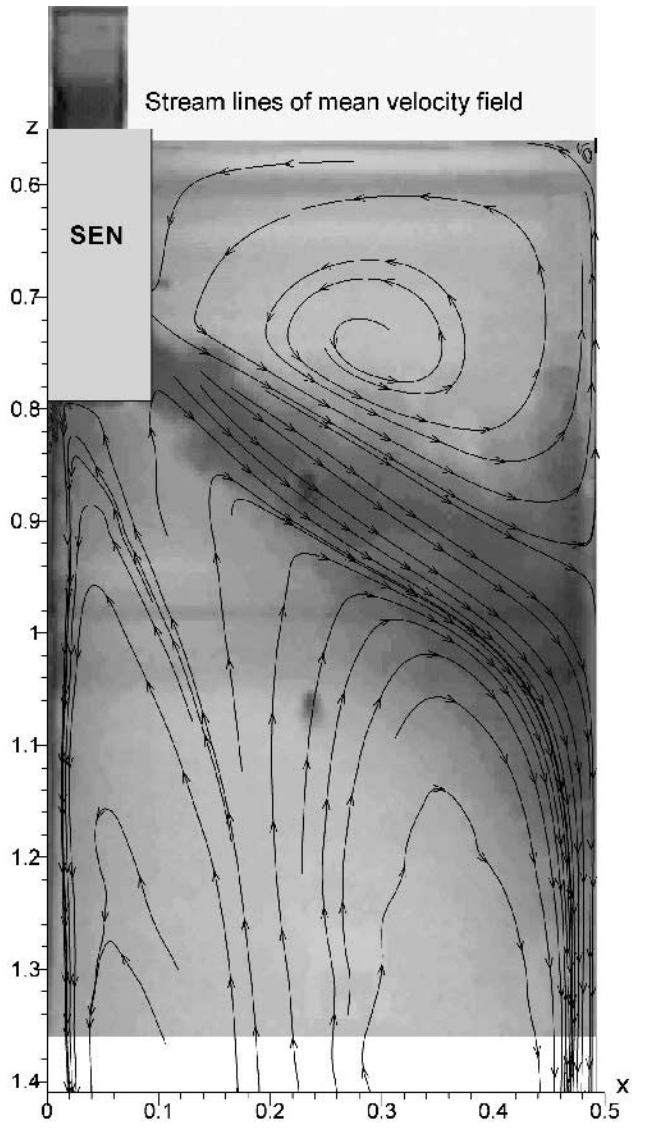

Fig. 13—Computed mean streamlines in the caster center plane superimposed on a photograph of the water model during dye injection.

temperature, containing almost all 57 °C of the superheat. The jets have very hot cores near the pouring temperature, but this quickly diffuses away. Most of the jet contains less than half of its original superheat. The temperature continuously drops as the molten steel moves farther from the nozzle ports, in proportion to increasing local residence time. The temperature in the upper-roll region is relatively uniform, with about 30 percent of its original superheat.

Figures 16 and 17 show the mean-temperature field in different cross sections through the domain. The temperature fields in these cross sections match the flow-field observations that there are large regions in the wall jet, center jet, and side jet where the temperature is fairly uniform at around 25 °C above the liquidus temperature.

The coldest regions in the temperature field are found near the solidifying shell and between the wall jet and the center jet low in the domain. Molten steel in the cooler interior contains only about a 10 °C superheat, because it slowly recirculates while it is cooled from both wide faces and there is no strong flow to carry in hotter steel. Except at its edges, the temperature of the top surface is relatively uniform, with an average superheat of about 20 °C. The most important part of the temperature field is the meniscus region, which comprises the perimeter around the top surface. The coldest part of the meniscus is at the top corner at the narrow face, caused by the small recirculation region there. The fluid here contains only 10 pct of its initial superheat, so it is 5 °C over the freezing temperature for the conditions here. The second-coldest part of the meniscus is the wide-face center plane, in the thin-flow region beside the SEN. If these meniscus regions get too cold, deep oscillation marks and subsurface hooks may form, leading to surface defects.

D. *Heat-Transfer–Model Validation*

To evaluate the accuracy of the heat-transport model, mean temperatures simulated in the upper-roll region were compared

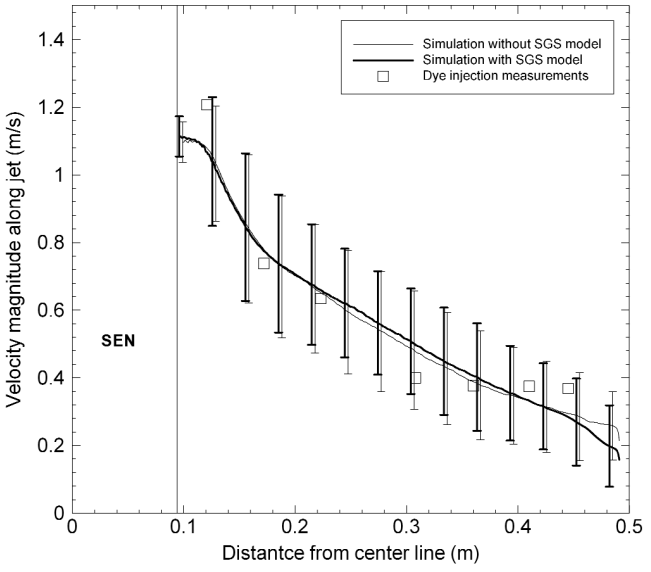

(*a*)

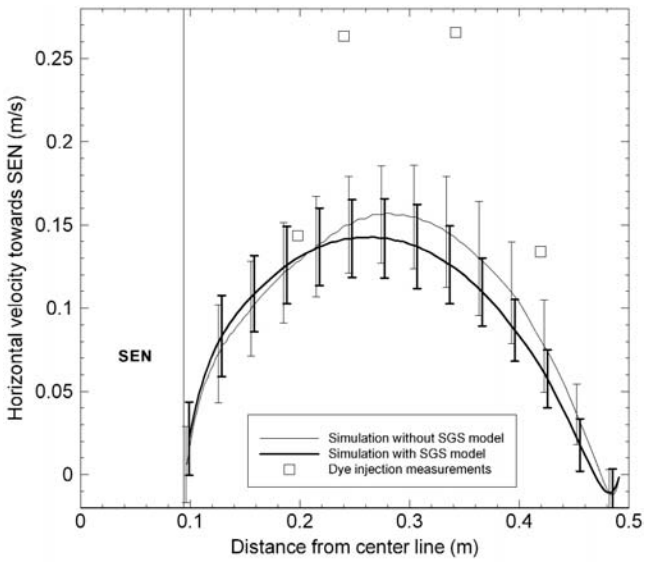

(*b*)

Fig. 14—(*a*) Velocity magnitude along the jet axis compared with dye-injection measurements and (*b*) top-surface velocity profile compared with dye-injection measurements.

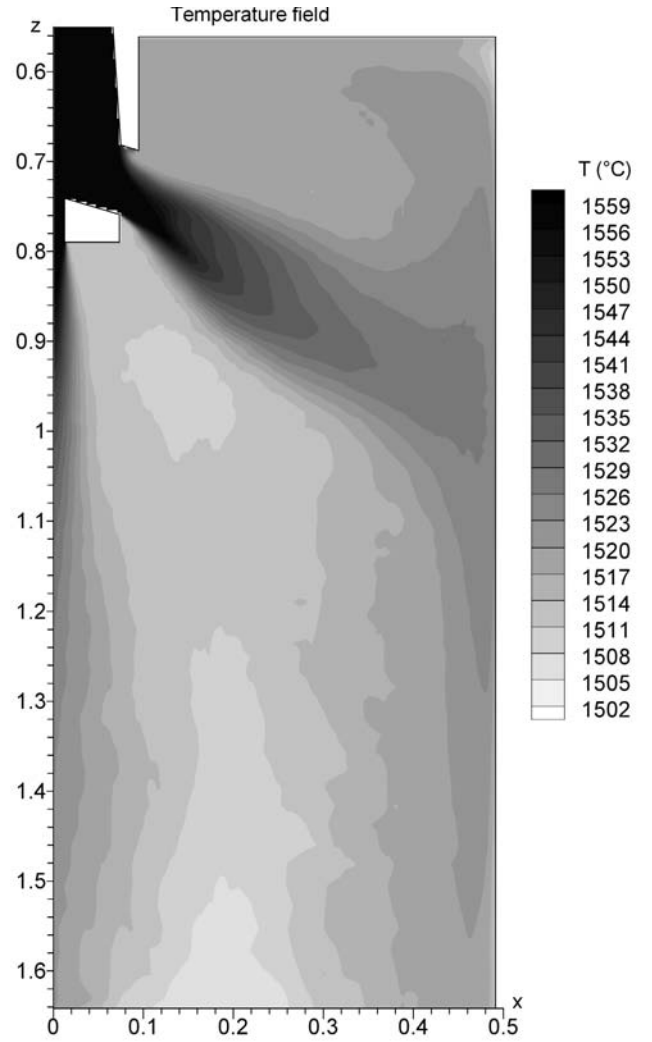

Fig. 15—Mean-temperature field in the *x*-*z* centerplane.

with plant measurements for the same geometry and casting conditions. Figure 18 shows the temperature along five vertical lines at different distances along the center plane of the caster. The measurements taken on insertion and withdrawal of the thermocouple probe compared very closely with predictions made both with and without the SGS model.

The temperatures were all near 1520 °C, which corresponds to 18 °C (or about 30 pct) of the superheat. The probe was unable to penetrate deep enough to enter the small region of the jet that is predicted to be appreciably hotter (Figure 15). Thus, the variations measured along each vertical line are small, except for inconsistent variations that appear to be due entirely to turbulent fluctuations. This is demonstrated by the differences between insertion and withdrawal. These variations are similar in magnitude to the RMS variations of roughly ±5 °C that are shown as error bars on the predicted curves.

The temperature variations across the mold are small with the exception of profile No. 4, 125 mm from the narrow face. The measured profile at this distance is colder than the others, which is expected due to the lower casting temperature for this experiment. Considering the direction of the flow pattern, it is unlikely that the temperature part way across the mold would be colder than that at either the adjacent narrow-face side or interior regions. In conclusion, these comparisons suggest that the temperature solution is accurate.

E. *Fluctuations in Velocity and Temperature Predictions*

The RMS statistics were calculated for 20 seconds after the flow field had reached a reasonably stationary state and after mean statistics already had been collected for 20 seconds. The largest velocity fluctuations occur at the edges of the jet near the nozzle. A contour plot of the RMS variation of the axial (*z*) velocity component is shown in Figure 19. The largest fluctuations reach ±0.27 m/s at the lower edge of the side jet. High-velocity fluctuations in the shear region are due to oscillations of the jet, which alternate between the fast jet and

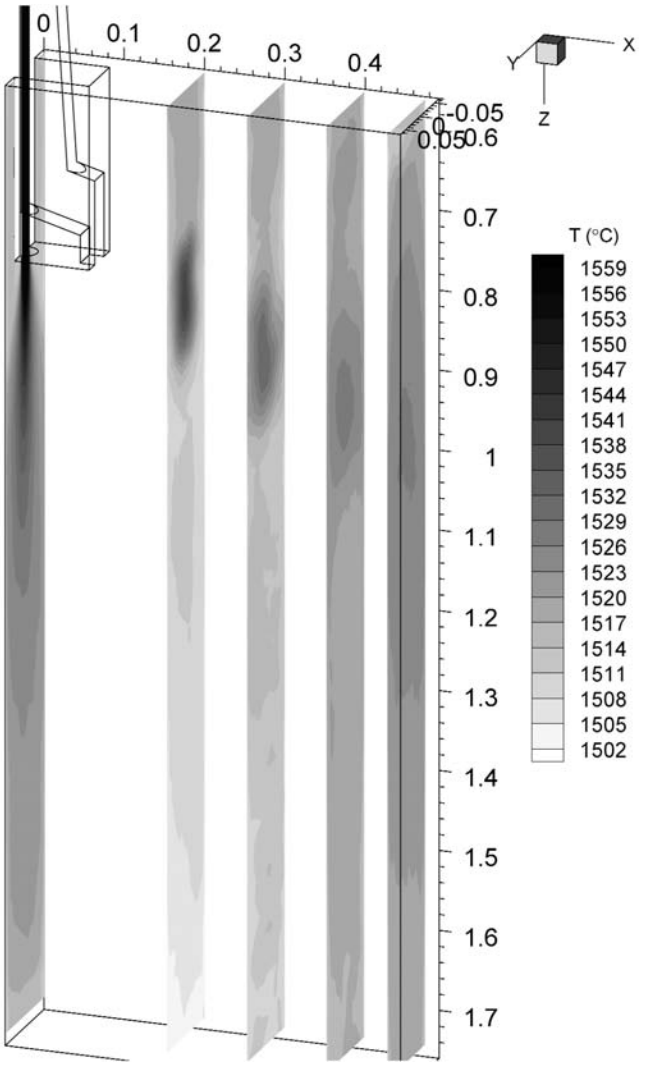

Fig. 16—Mean-temperature fields in cross sections parallel to the narrow face.

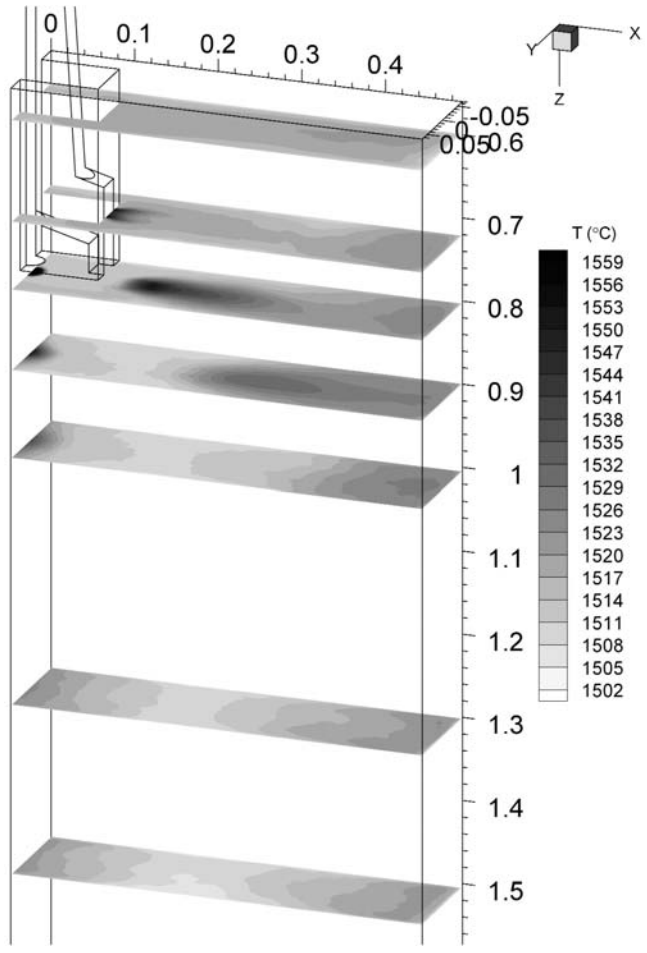

Fig. 17—Mean-temperature fields in cross sections parallel to the top surface.

the relatively stagnant surrounding fluid. The edges of the central jet also experience high fluctuations.

The fluctuations of all three velocity components are generally similar. Figure 20 compares the RMS velocity components in the *x*, *y*, and *z* directions along a vertical line that passes through the jet. The axial components experience the largest fluctuations, while the *y*component perpendicular to the jet is smaller. Two regions near the nozzle experience the largest fluctuations. At the top of the side port, where the flow turns direction at a sharp corner, the u-velocity RMS is very large. At the lower edge of the side port and at the exit from the central port, the flow separation generates large RMS components. These details of the flow characteristics exiting the nozzle are important because they control the flow pattern in the entire mold.

Although smaller than in the port region, the interior of the jet also experiences significant velocity fluctuations. Specifically, the RMS of all velocity components ranges from 0.15 to 0.20 m/s, which exceeds ~25 pct of the mean velocity. Near the impingement region, the RMS of the *v*-velocity component is largest, indicating strong oscillations of the jet over the narrow-face wall. Lower in the caster, the velocity fluctuations of ~0.1 m/s are on the same order as the velocities themselves. These fluctuations have an important effect on particle motion and mixing. Further details on the RMS velocity profiles are presented elsewhere.[22,29]

Like the behavior of the velocity variations, temperature fluctuations are also largest at the edges of the jets, especially near the nozzle. Figure 21 shows the RMS of temperature in the center plane. The RMS of temperature peaks at the edge of the jet at 14 °C. In the upper-roll region and wall-jet region, the fluctuation of temperature is generally below 3 °C. Near the solidifying shell, the temperature fluctuation is around 5 °C. These temperature fluctuations greatly change the heat flux imparted to the solidifying shell. This indicates the importance of turbulence in the transport of superheat to the solidifying shell.

F. *Instantaneous Velocity and Temperature Fields*

Transient features of the steel-flow and heat-transfer phenomena are very important to the understanding of continuous casting processes. In addition to the RMS statistics, dynamic structures in the velocity and temperature fields are revealed by snapshots and animations.

Figure 22 shows the center plane of a typical instantaneous flow field. This snapshot generally resembles the mean flow field in Figure 8. However, the unique flow structures reveal

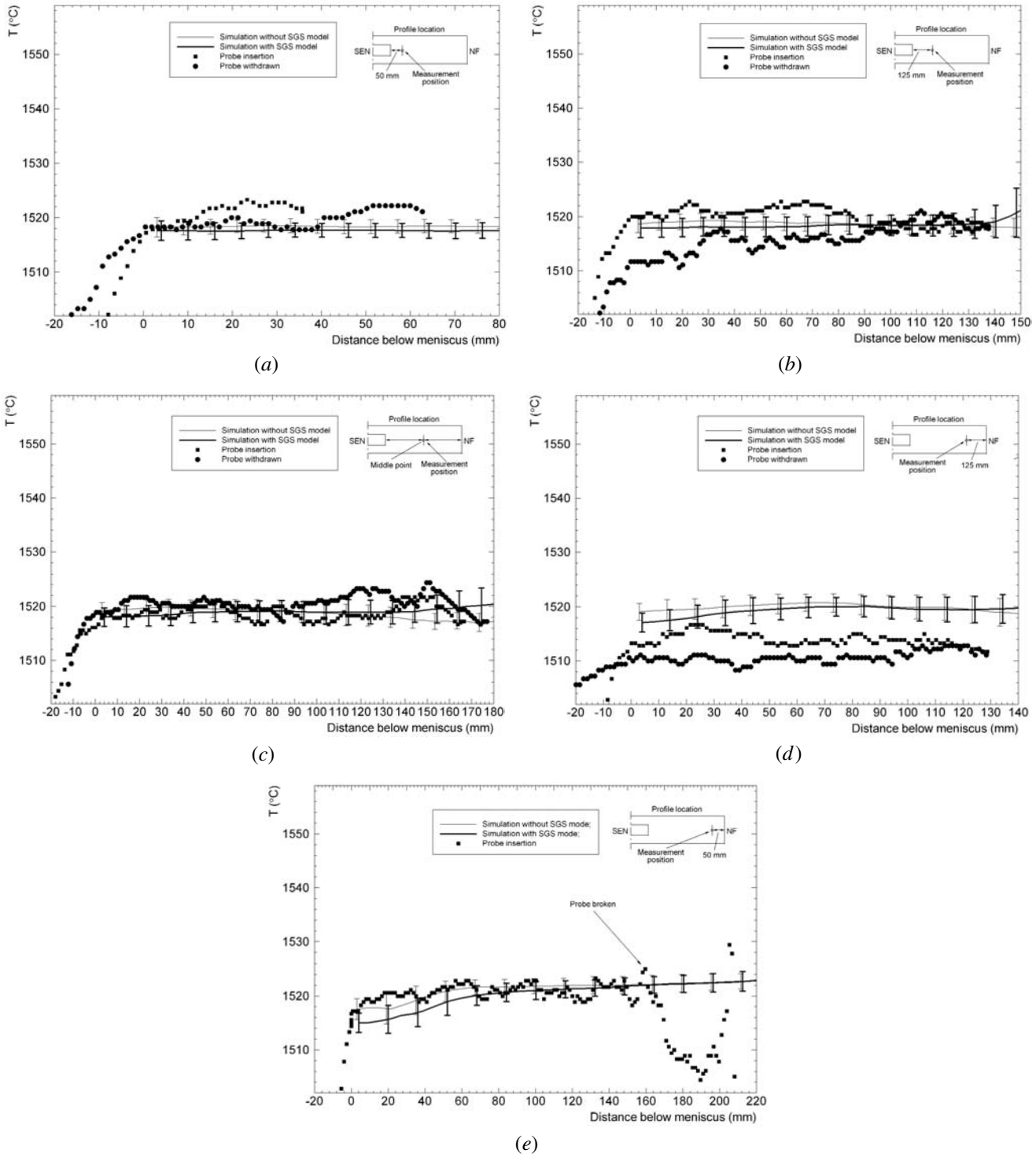

Fig. 18—Comparison of simulated temperature profile and plant measurements: (*a*) measurement 1: 150 mm from the centerline; (*b*) measurement 2: 225 mm from the centerline; (*c*) measurement 3: 295 mm from the centerline; (*d*) measurement 4: 365 mm from the centerline; and (*e*) measurement 5: 440 mm from the centerline.

interesting differences. Many small vortices are generated at the edge of the jets due to shear with the surrounding fluid. These vortices are advected with the flow, causing oscillation of the jet. This tends to destabilize the flow pattern with increasing distance from the nozzle. While the upper-roll region often is comprised of a single large vortex, at other times it breaks up into several smaller vortices.[22]

Figure 23 shows the corresponding instantaneous temperature field in the center plane. The high-temperature core of each jet quickly diffuses as swirls of colder fluid are intermittently entrained. Convective mixing due to the chaotic motion of the vortices in the upper roll keeps the region above the side jet at a fairly constant temperature, ~20 °C above the liquidus.

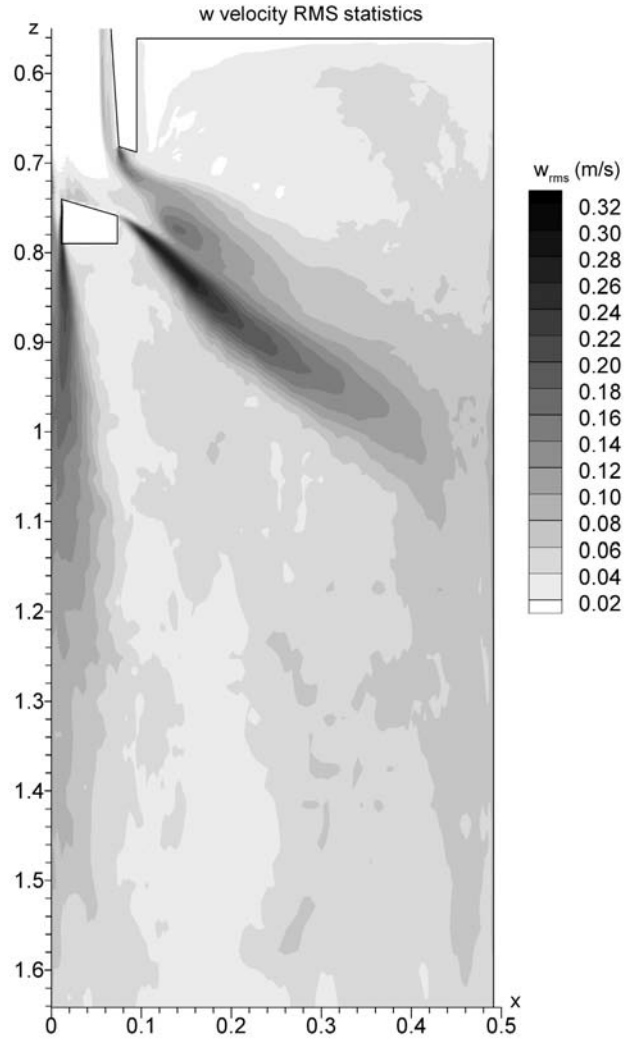

Fig. 19—Axial velocity variations (z direction RMS statistics) in the centerplane.

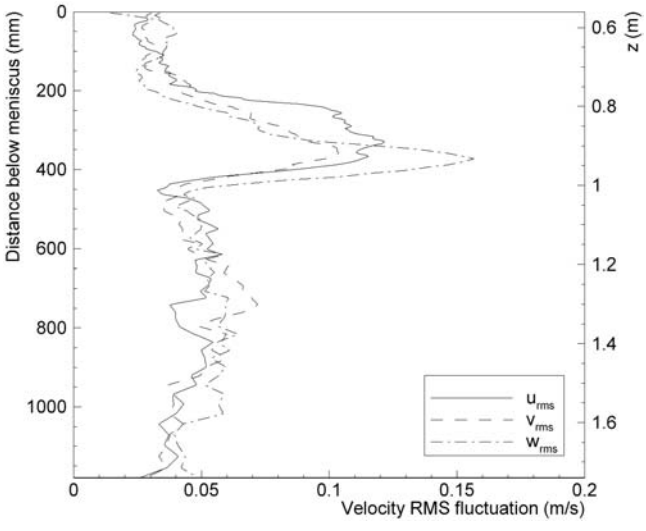

Fig. 20—Comparison of velocity fluctuations in the x, y, and z directions along a vertical line in the centerplane located 0.2 m from the nozzle.

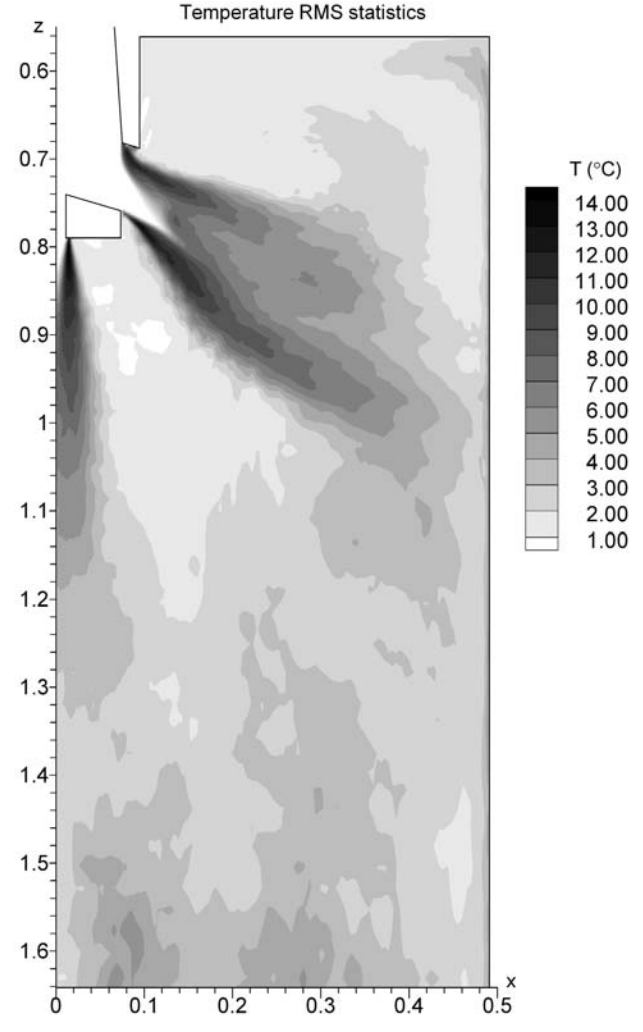

Fig. 21—Temperature variations (RMS) in the centerplane.

Figure 24 shows instantaneous velocity and temperature fields in vertical cross sections in the y-z plane. Figure 24(a) shows typical instantaneous flow and temperature fields in the symmetry plane between narrow faces. Flow from the center port in the nozzle creates asymmetrical vortices. The confined jet oscillates between touching one wide face and then the other.

In the cut through the side jet (Figure 24(b)), the vortices interact with the slower downward recirculating flow from the upper roll. Even though the geometry and simulation domain are perfectly symmetrical, significant instantaneous asymmetry develops due to its turbulent nature. Sometimes, symmetrical vortices are generated on both sides of the jet, but usually the jet contains multiple asymmetric swirls. The asymmetry is caused by oscillation of the jet between the wide faces, as it traverses the mold. From the animation of the flow field, the oscillation frequency is estimated to be 5 to 10 Hz. The temperature field inside the jet exhibits intermittent oscillations and sharp localized spikes as well. The temperature field above the jet, which is in the upper-roll region, is fairly uniform. The temperature below the jet is one of the coldest regions in the domain. The solidifying wide faces and the lack of influence from the hot jets

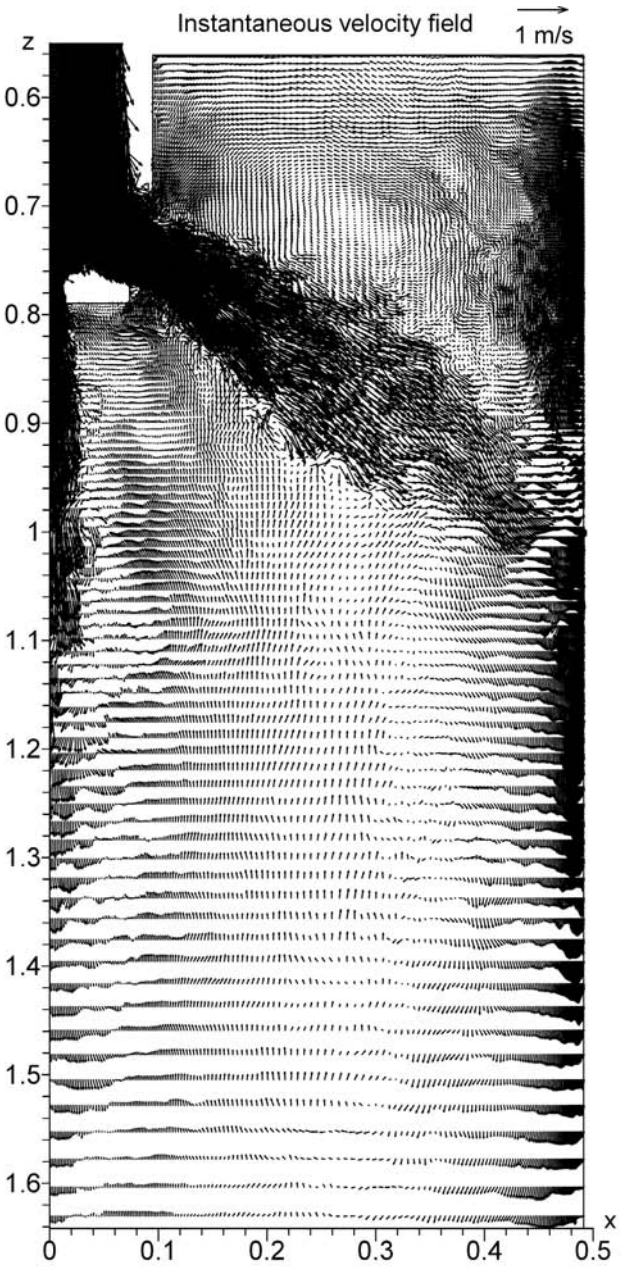

Fig. 22—Instantaneous velocity-vector plot in the caster centerplane.

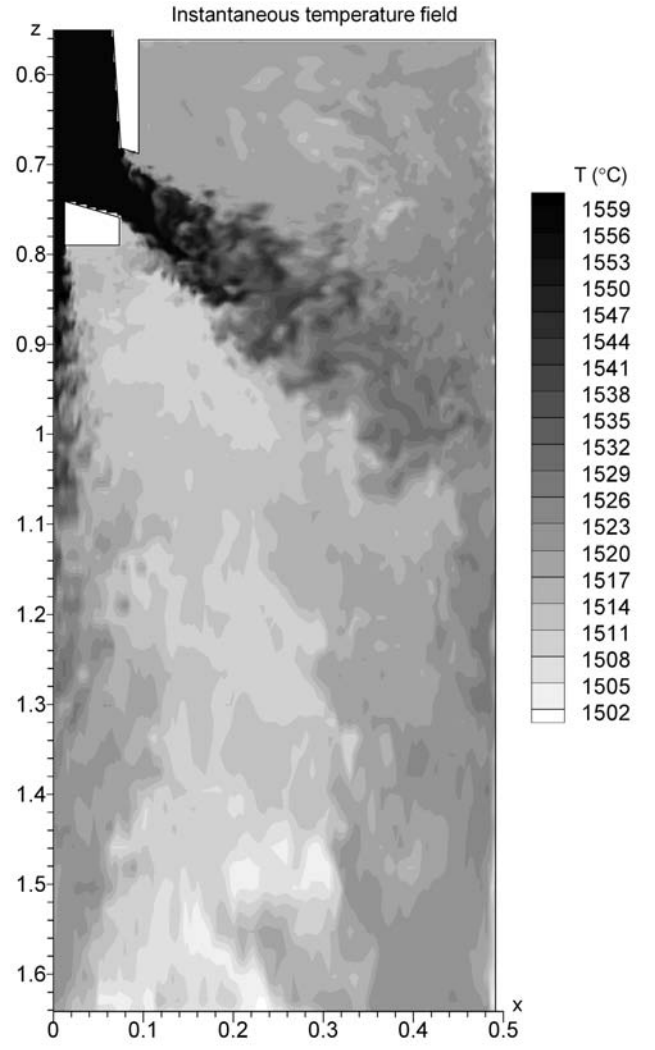

Fig. 23—Instantaneous temperature field in the caster centerplane.

cool this region to only a few degrees above solidification temperature.

In the cut through the wall jets (Figure 24(c)), flow in the lower region is seen to be greater down the corners, owing to the spreading at the impingement point shown in Figure 10. Despite the complex flow patterns, the instantaneous temperature is fairly uniform at around 25 °C above the liquidus temperature. Near the top corner, the recirculation region that causes the important temperature drop at the meniscus (as discussed earlier) changes greatly with time. This is more easily seen in the transverse cross section in Figure 25(a), cut 38.5 mm below the top surface. This snapshot shows how the vortices penetrate intermittently due to chaotic bursts of strong flow caused by oscillation of the jet. Corresponding portions of the meniscus are very cold and vary in time and position. Thus, although the time-averaged results show that the narrow-face and SEN centerline regions are colder on average, defects related to instantaneous cold spots are intermittent and could be found anywhere around the shell perimeter.

Figure 25(b) shows instantaneous velocity and temperature fields in a transverse section 243 mm from the top surface. This view cuts through the central jet, the side jet, and the upper wall jet. The complex vortices associated with the shear and oscillation of the side jet are revealed. The oscillation frequency of the side jet is also about 5 to 10 Hz. There are also strong vortices near the narrow face where the wall jet goes up, indicating its helical structure. The spiral motion at the corner of the wall jets, shown as time-averaged recirculation zones in Figure 12, are revealed in the instantaneous plots such as Figure 25(b) to actually consist of a complex evolving structure of vortices. In addition to the larger velocities up to 0.1 m in diameter, the wall jet also includes vortex structures smaller than 0.01 m. Even the largest vortices are generally short lived, lasting ~0.5 seconds. The temperature in the core of the jets exhibits hot spikes. The region between the side jet and the central jet is relatively cold. In the upper recirculation region to the right-hand side of the jet core, the temperature is higher and fairly uniform.

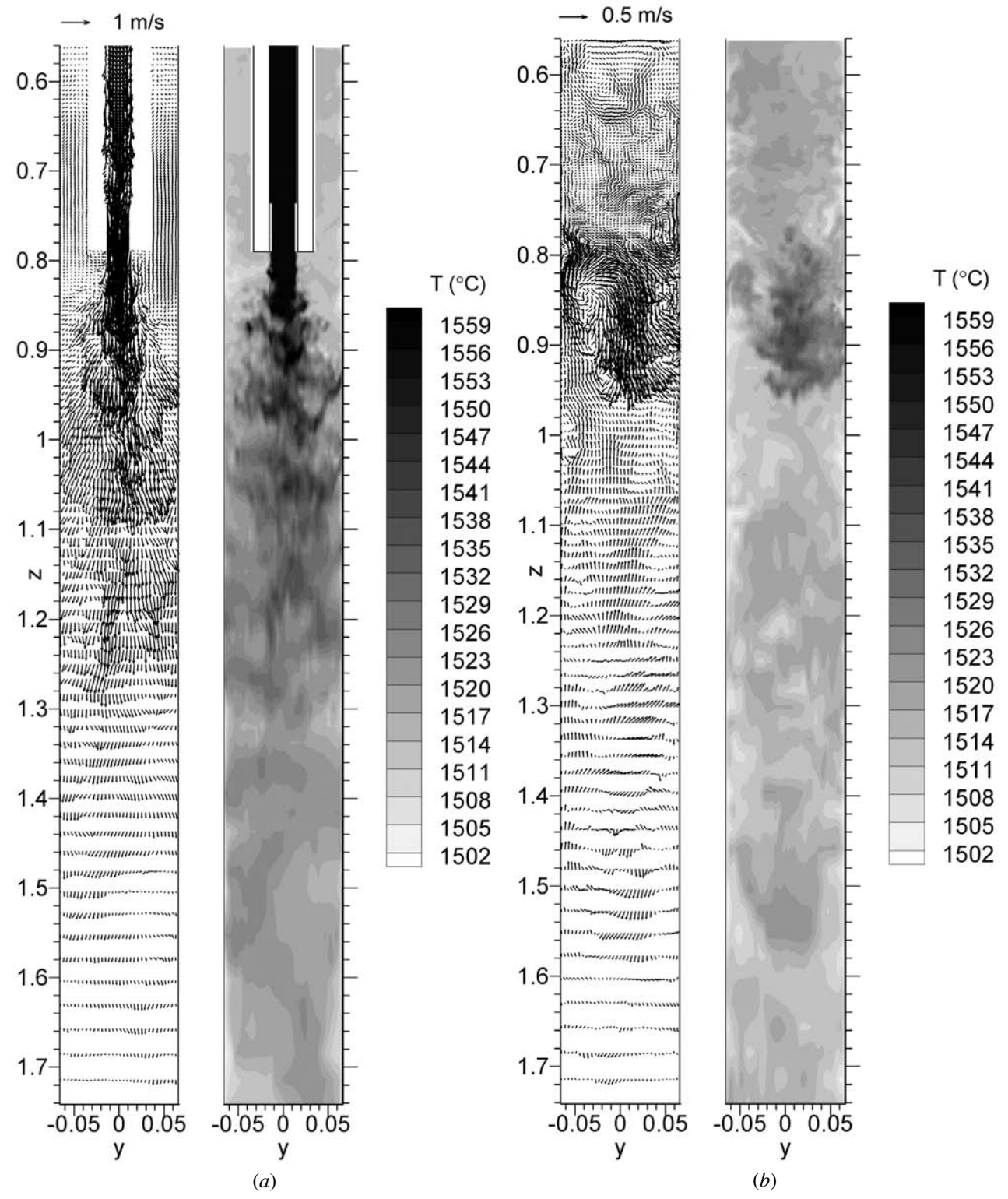

Fig. 24—Instantaneous velocity and temperature fields in vertical *x-z* cross sections parallel to the narrow face: (*a*) cut showing the jet from the central port in the center plane between the narrow faces, (*b*) cut through the side jet 192 mm from the narrow face, and (*c*) cut through wall jets 93 mm from the narrow face.

Figure 25(c) shows results in a cross section through the lower recirculation region, 741 mm below the top surface. The central jet has spread. Although still complex, the instantaneous vortex structures of the wall jet show the same two counter-rotating vortices found near the corners in Figure 12. They are generally larger, slower, and colder at this far distance 376 mm below the impingement point. These vortices from the central and wall jets strongly influence the mixing and temperature in this region, as they bring faster, hotter fluid into this otherwise cold stagnant region. In the animation

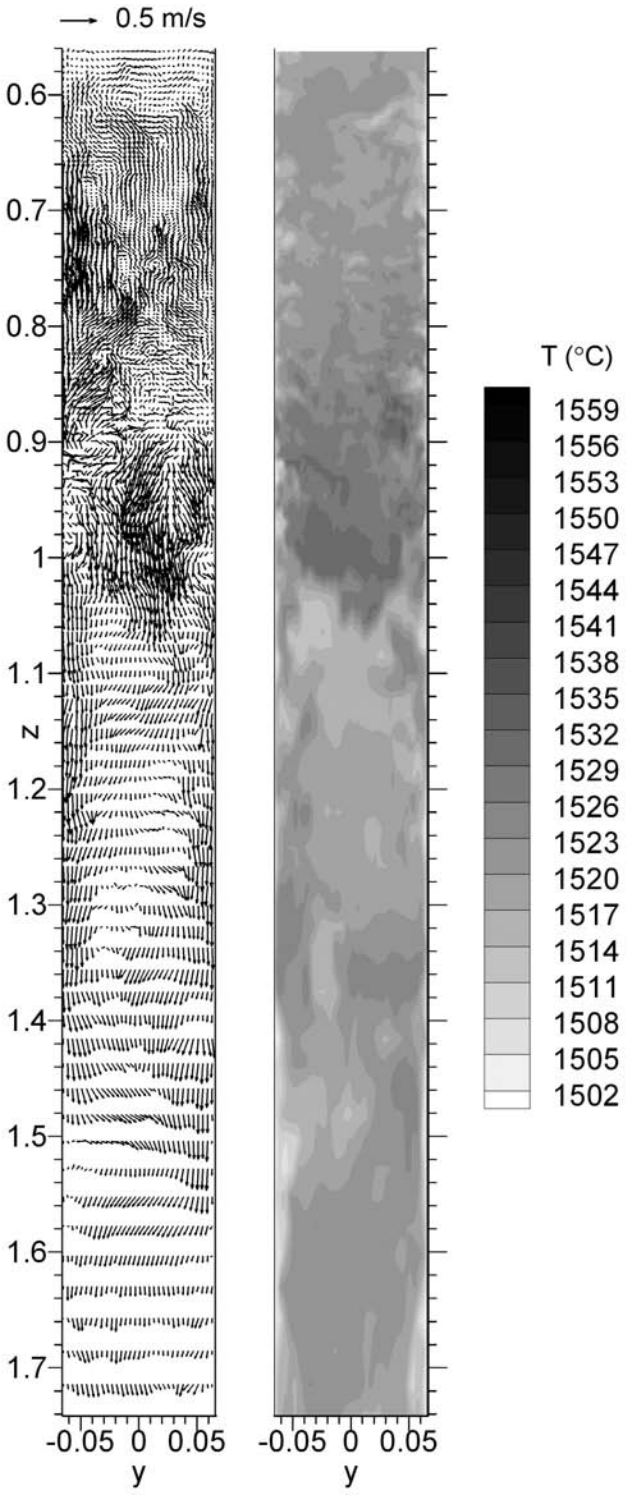

(*c*)

Fig. 24—(Continued). Instantaneous velocity and temperature fields in vertical *x-z* cross sections parallel to the narrow face: (*a*) cut showing the jet from the central port in the center plane between the narrow faces, (*b*) cut through the side jet 192 mm from the narrow face, and (*c*) cut through wall jets 93 mm from the narrow face.

of the flow field, the large vortices break down into small vortices and then merge together again. The vortices here last longer than the ones higher in the mold, because they are further from the rapid transient effect of the jets.

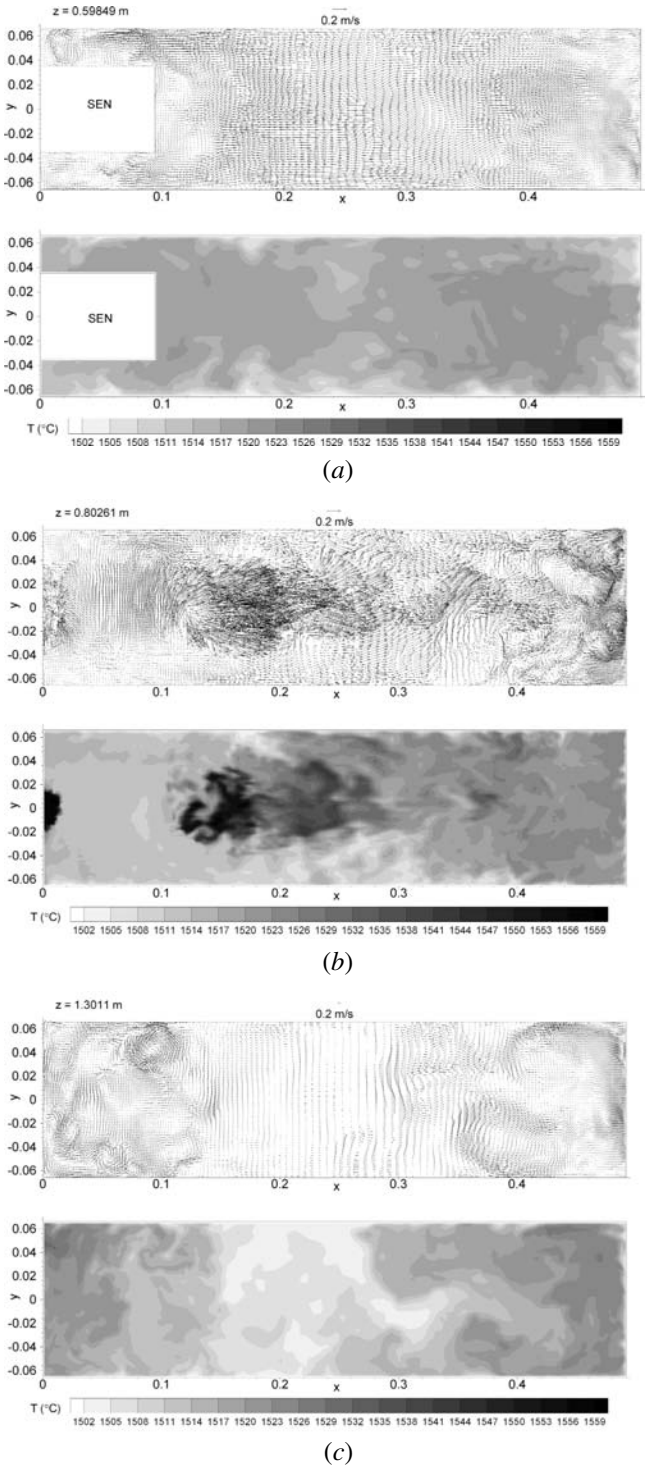

(*a*)

(*b*)

(*c*)

Fig. 25—Instantaneous velocity and temperature fields in horizontal *x-y* cross sections (*a*) 38.5 mm from the top surface, (*b*) 243 mm from the top surface, and (*c*) 741 mm from the top surface.

G. *Heat-Transfer Rate to the Solidifying Shell*

The average rate of superheat flux to the inside surface of the solidifying steel shell is shown in the contour plots of Figure 26. Results over the two symmetrical wide faces were averaged. The heat-flux profiles along three different vertical lines are given in Figures 27 through 29. The heat flux is largest where the side jet impinges on the narrow

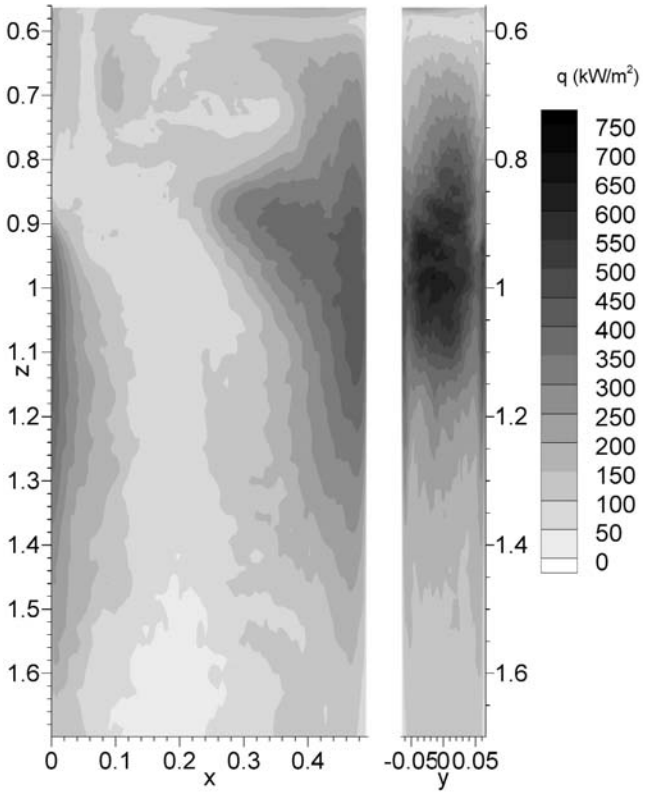

Fig. 26—Time-averaged heat fluxes through two solidifying faces.

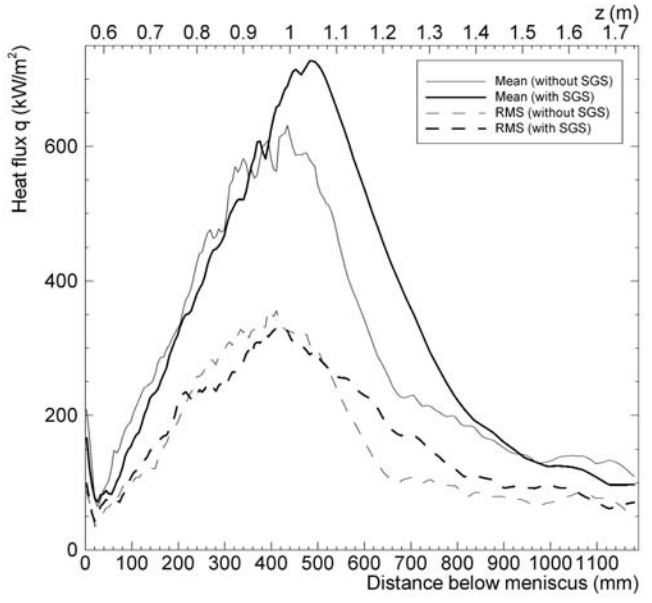

Fig. 27—Mean heat flux along the centerline of the narrow face.

face, reaching a maximum of almost 700 kW/m^2. This heat flux is significant, because it can slow down solidification of the shell, especially where there is also an interfacial gap that limits the removal of heat from the shell.[33] In extreme cases, this can cause a breakout, where molten steel drains through a rupture of the resulting thin spot in the shell.[34]

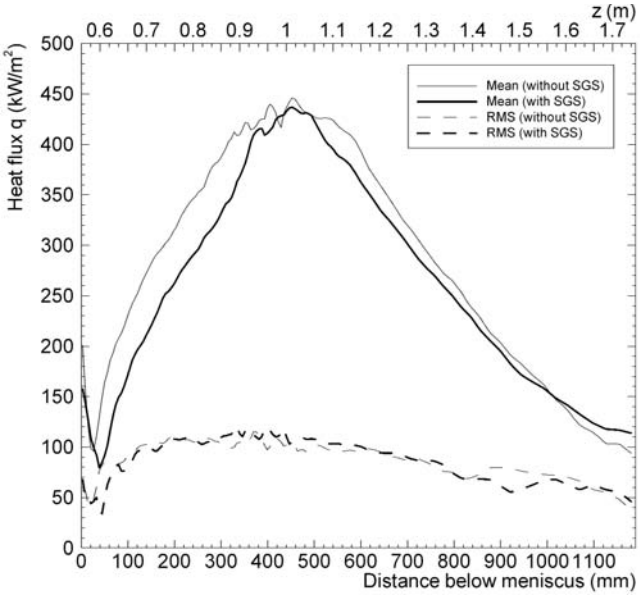

Fig. 28—Mean heat-flux profile along a vertical line on the wide face (20 mm from the narrow face).

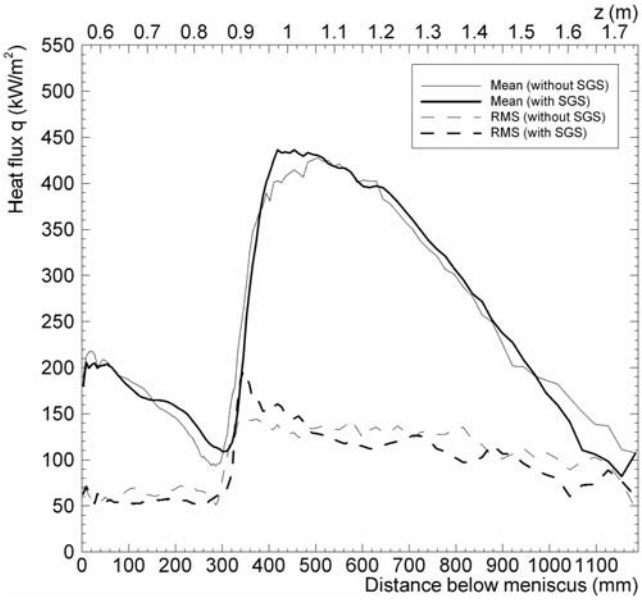

Fig. 29—Mean heat flux along the centerline of the wide face.

The high-heat-flux region along the narrow face is not positioned symmetrically about the impingement point. Instead, Figure 27 shows that the profile is skewed toward the lower side of the impingement point, which was also observed in the experimental study of an oblique impinging jet by Goldstein.[35] This also agrees with previous computations of heat flux in continuous-casting molds.[13,18] Figure 27 also shows that the heat flux at the meniscus reaches a peak of about 200 kW/m^2. The heat flux just below the meniscus drops sharply to less than 100 kW/m^2 on the narrow face, owing to the depletion of sensible heat from the molten steel in the small recirculation region near the top of the narrow face. The heat flux at the meniscus also reaches

200 kW/m^2 between the SEN and the narrow face, due to the higher velocities across the top of the upper roll, and near the centerline between the SEN and wideface, due to the vortices generated as flow goes around the SEN.

On the wide faces, there are large areas where the average heat flux exceeds 350 kW/m^2. These coincide with contact of the spreading central and side jets against the wide faces. As shown in Figure 28, heat flux to the wide face reaches a maximum of 450 kW/m^2 near the narrow-face corner, where the strong spiral vortices generated by the impinging side jet spread around the edge where the narrow face and wide face meet.

The heat-flux distribution fluctuates considerably in time, as evidenced by the large values of the RMS heat flux, which are included as error bars in Figures 27 through 29. The RMS values often exceed 40 pct of the mean heat flux, reaching a maximum of 350 kW/m^2 at the impingement region on the narrow face. The RMS variations in heat flux are consistent with trends of the velocity RMS.

Figure 30 shows contours of the instantaneous heat flux to the shell at both the wide face and narrow face. In contrast with Figure 26, the impingement region is shown to actually consist of multiple impingement points. Heat flux in the impingement region is generally lower than the mean, but contains sharp localized spikes that exceed 1500 kW/m^2 at many points on the narrow face. The instantaneous heat flux exceeds 900 kW/m^2 on the wide face. These instantaneous heat-flux peaks exceed twice the mean and change rapidly in both time and space due to the oscillation of the jet and the turbulent eddies it contains. Oscillations occur from wide face to wide face as well as in the casting direction. Elsewhere on the shell surface, where the jet is closer to the nozzle, the variations are smaller. In these regions, the RMS heat flux is a smaller fraction of the total heat flux.

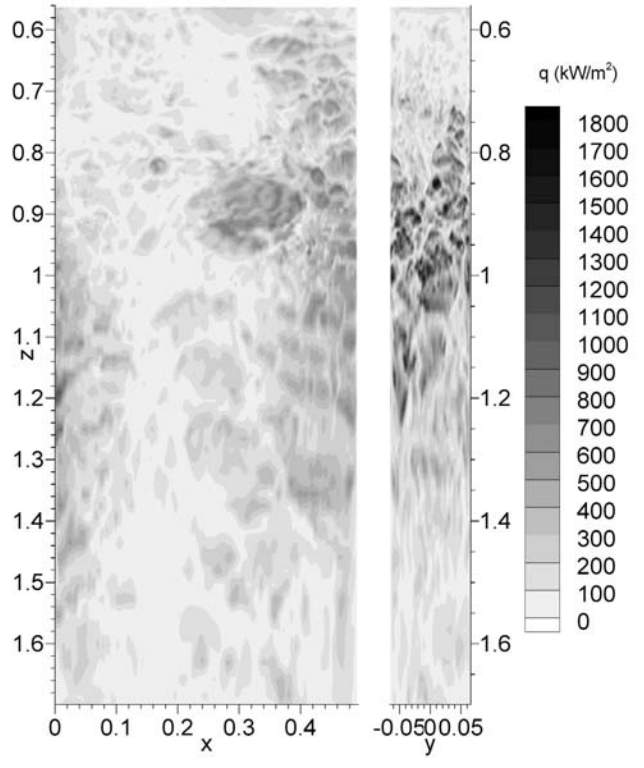

Fig. 30—Instantaneous heat fluxes through two solidifying faces.

H. *Heat Balance*

According to the boundary conditions of the simulation, superheat carried by the molten steel enters the domain through the nozzle inlet. This heat can leave the domain through the solidifying shell or through advection with the liquid flowing out of the domain bottom toward the lower regions of the caster. The superheat transferred to the solidifying shell is of particular interest to this study, especially near the meniscus where the surface is formed.

The superheat represents the sensible heat contained in the liquid steel and is of important metallurgical interest. The superheat is defined as

$$Q = \int \rho C_p (T - T_0) dV \qquad [12]$$

where T_0 is the liquidus solidification temperature of the steel. Solidification is not modeled in this simulation, so the latent-heat evolution of liquid steel occurs outside the domain and is not considered.

During the statistically stationary stage of the simulation, a pseudosteady state is achieved. The superheat entering and leaving the domain forms a dynamic balance, meaning that it must balance on average. Due to the transient nature of the flow and heat transfer, this equality is not necessarily satisfied at each time instant. This causes the superheat to fluctuate with time by ± 0.4 MJ, which is about 8 pct of the average. The mean superheat is 5.41 MJ and 5.06 MJ for the 40-second simulations without and with the SGS model, respectively. The difference between models is not surprising, because the total energy has fluctuation frequencies lower than 0.025 Hz. Minor differences between any two averages over a 40-second time period are, thus, expected.

A detailed superheat budget can be calculated from the mean flow and temperature fields. The rate of superheat entering or leaving the domain through advection across the inlet and outlet boundaries can be calculated by

$$\dot{Q}|_{inlet} = \int \rho C_p (T - T_0) V dA \qquad [13]$$

where V is the velocity normal to the inlet or outlet surface. Note that this average rate is not exactly the simple product of average temperature and average velocity. This is because Eq. [12] includes fluctuating components, which could be represented as an extra term, $\overline{T'V'}$. This term represents the turbulent heat flux, which is zero at the inlet where there is no temperature variation, but is a significant fraction of the heat leaving the domain.

The rate of superheat leaving through the solidifying shell is calculated by integrating the heat flux (q) over the narrow and wide faces:

$$\dot{Q}|_{\text{wall}} = \int q dA \qquad [14]$$

Averaging these quantities over 40 seconds, the total superheat entering the domain is 449 kW. The heat leaving through the walls is 44 kW from the narrow face and 111 and 106 kW from the wide faces. The heat leaving the domain is 189 kW, which includes 29 kW for the turbulent component. Although the narrow face has a 1.5-times-larger peak-heat flux and

5-times-larger mean heat flux, more heat leaves through the wide faces, owing to their 7.45-times-larger surface area.

In the real casting process, heat is also lost through the liquid flux and powder layers that float on top of the molten steel. For the conditions of this work, given in Table III, heat loss via conduction is estimated to be about 330 kW/m^2 for a 5-mm-thick liquid flux layer. Based on computations elsewhere,[27] there should be negligible natural convection in the liquid flux, and Nu should be 1.1. Multiplying the product of these by the surface area of 0.0563 m^2 gives a rate of superheat loss through the top surface of about 20 kW, which represents 4.5 pct of the superheat entering the domain. Considering the variations and uncertainties in flux-layer thickness, velocity gradients, and flux properties, this fraction is estimated to range from 2 to 6 pct. Although not important to the results presented in this work, this heat loss is likely very important to meniscus hook formation and other phenomena that affect initial solidification and surface defects.

The superheat budget is summarized in Figure 31. About 64 pct of the superheat leaves through the solidifying shell in the mold (the top 1200 mm of the caster). This value would be even larger if the increase in shell thickness down the mold were taken into account. About 35 pct of the superheat is extracted below the mold lower in the caster (below the domain). These values are comparable to previous findings[13] that most of the superheat is extracted in the mold.

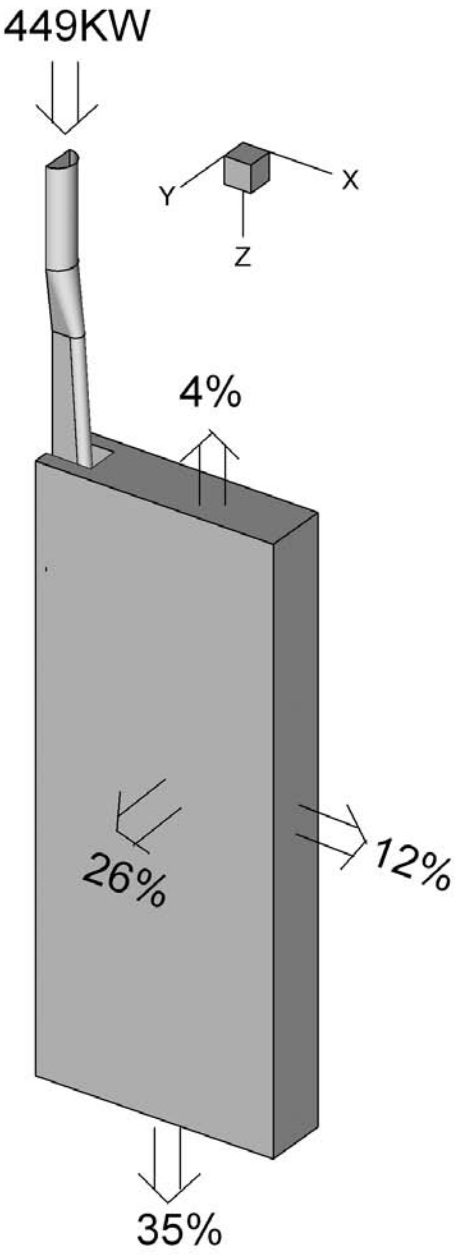

Fig. 31—Superheat removal distribution.

I. *Effect of SGS Model*

Including the SGS *k*-model influences the flow pattern somewhat, especially in regions of high turbulence, as expected. The flow fields at the nozzle exit are compared in Figure 32 with and without the SGS model. Although both simulations show the same general features, the swirl is weaker without the SGS model, allowing recirculating flow to extend across the entire top of the side port. This is due to the smaller viscosity without the SGS component. The mass flow through the ports is virtually the same for both cases, with flow through the side ports comprising 84.6 and 84.9 pct of the total flow rate for cases with and without the SGS model, respectively. However, the flow pattern in the low-velocity region just outside the port is different with the SGS model. Specifically, the extra flow through the top of the port causes the high-velocity region of the jet to extend higher, leading to a wider, more-diffuse jet. Without the SGS model, a narrower jet penetrates straighter into the mold cavity, which matches better with observations of the water model. The difference between models decreases with distance from the nozzle.

The velocity and temperature predictions with and without the SGS model are compared in Figure 33. The small differences generated at the nozzle cause the downward jet angle to increase to 29 deg with the SGS model, which, in turn, makes the impingement point 15 mm lower and the eye of the upper roll 30 mm higher. The increased diffusion also causes the velocity RMS statistics to decrease with the SGS model. In the extreme, velocity fluctuations near the narrow face are almost half those without the SGS model.

The temperature fields also reflect the subtle difference in diffusion between models. Including the SGS model produces a slightly lower temperature in the top part of the liquid pool. Similarly, the downward wall jet becomes colder, as this jet looses heat faster with the SGS model. However, as shown in Figure 18, the difference between results of the two models is small, so both predictions agree equally well with the measurements. Figure 18(b) shows that the temperature profile turns upward slightly at a 150 mm depth for the SGS model, as the upper region of the jet is just penetrated.

The effect of the SGS model on heat flux is included in Figures 27 through 29. Except at the impingement point on the narrow face, the SGS model has no significant effect on heat transfer. The SGS diffusion added by the SGS model (mainly near the nozzle) causes the side jet to deliver about 10 pct more heat flux to the narrow face at and below the impingement point. This explains the lower temperatures found where the colder wall jets later travel. The RMS values are very similar with and without the SGS model. Thus, the SGS model does not appear to have much influence on the

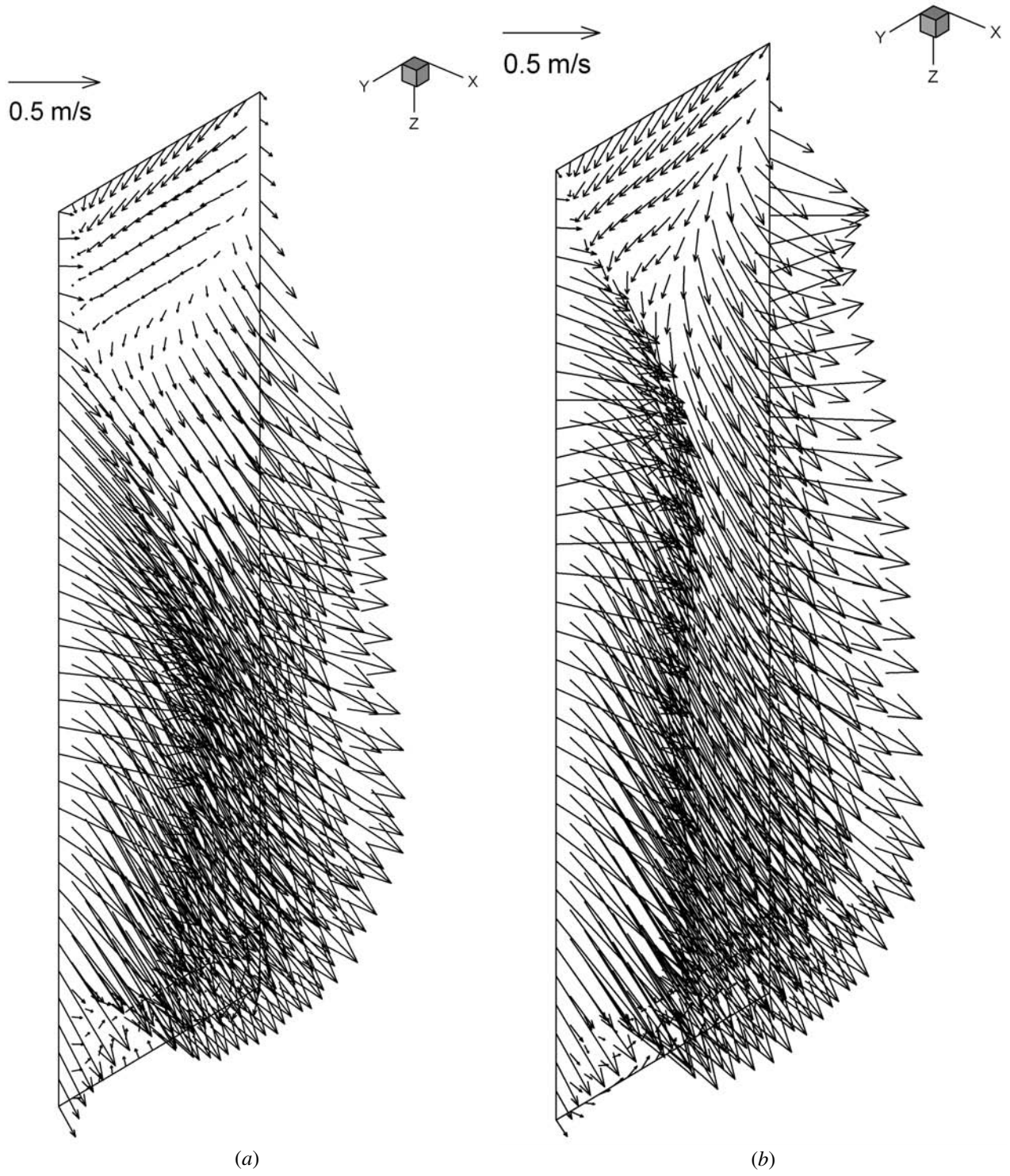

Fig. 32—Velocity distribution at the nozzle side-port exit plane (*a*) with the SGS model and (*b*) without the SGS model.

solution. Further investigation of the computational aspects of this simulation are given elsewhere.[36]

VII. SUMMARY

A 3-D LES code, UIFLOW, was applied to compute turbulent single-phase flow, temperature, and superheat flux in the liquid-steel pool region of a continuous slab caster. The computational model has 1.6 million nodes and is validated through comparison with previous measurements of heat transfer during the impingement of an air jet on a cooled flat plate. The simulation results agree with both dye-injection measurements of velocity in a full-scale water model and thermocouple temperature measurements in the upper region of the mold in an operating steel caster. At 1.52 m/min,

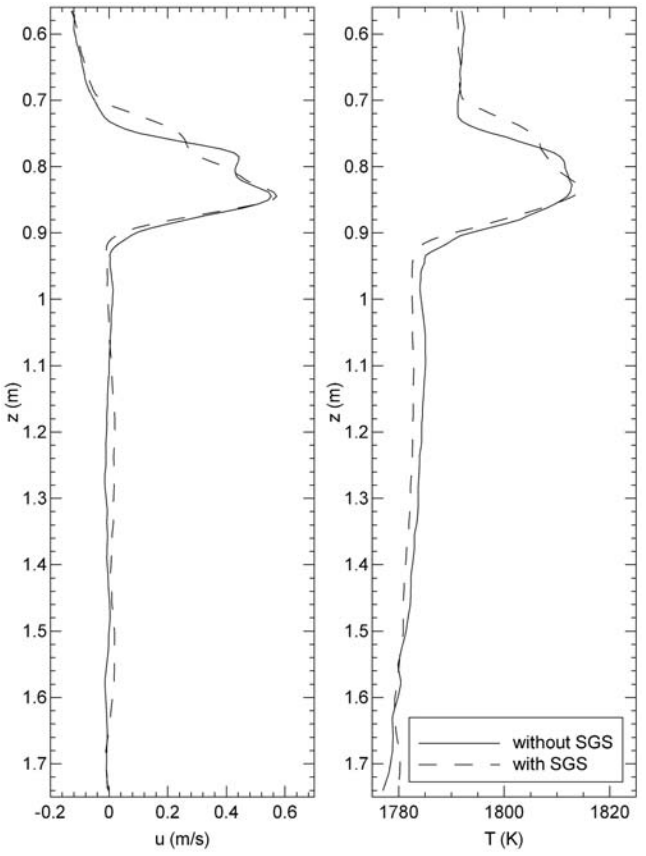

Fig. 33—Effect of the SGS model on mean *u*-velocity and temperature profiles in the center plane, 292 mm from the narrow face.

the 132 × 984 mm caster exhibited a classic double-roll flow pattern, with about 85 pct of the flow leaving the two larger side ports of a three-port nozzle. Animations of the flow and temperature field give insight into the transient flow structures and the transport of superheat in the mold region.

Although the domain and grid were symmetrical, asymmetric jet behavior was observed. The side jet shows strong oscillations between the wide faces, with frequencies on the order of 5 to 10 Hz. The wall jets generate spiral vortices near the edges between the wide and narrow faces, with life spans shorter than 1 second. This swirling motion helps to maintain relatively uniform temperature in the jets and upper recirculation regions, where temperatures fluctuate only ±4 °C from their average of 30 pct of the initial superheat-temperature difference entering the mold.

The largest rate of superheat transport to the dendritic surface of the solidifying steel shell is at the impingement region of the side jet onto the narrow face, where the mean reaches about 700 kW/m^2, with instantaneous local spikes exceeding 1500 kW/m^2 and RMS variations reaching ±350 kW/m^2. High local heat-transfer rates are also found elsewhere on the wide faces, where the jets spread to contact the solidification front. A small but persistent recirculation region is observed at the narrow-face meniscus, which decreases the local temperature just below the meniscus. The superheat transport to the meniscus region is about 200 kW/m^2. About two-thirds of the superheat is extracted in the mold, including 12 pct going to the narrow faces, for the conditions simulated. The extra diffusion added by the SGS static-*k* model affects the flow and heat transport slightly, when that model is employed.

ACKNOWLEDGMENTS

The authors thank the National Science Foundation (Grant No. DMI-01-15486) for the support that has made this research possible. This work is also supported by the member companies of the Continuous Casting Consortium at the University of Illinois at Urbana–Champaign (UIUC). Special thanks are due to Ya Meng and Tiebiao Shi for help with the plant measurements and to the National Center for Supercomputing Applications (NCSA) at UIUC for computational facilities.

APPENDIX

Numerical method

A finite-volume method was used to solve Eqs. [1] through [3]. Central differencing with second-order accuracy was used to discretize the equations on a collocated grid with variables defined at the cell centers. The time integration of the equations was done using a semi-implicit, fractional-step method treating diffusion terms implicitly by the Crank–Nicolson method. The convective and source terms from SGS stresses are advanced explicitly using the second-order Adams–Bashforth method. After applying the semi-implicit procedure, the momentum equations take the following form:

$$\frac{\bar{u}_i^{n+1} - \bar{u}_i^n}{\Delta t} = \frac{3}{2} H_i^n - \frac{1}{2} H_i^{n-1} + \frac{1}{2\rho_0} \frac{\partial}{\partial x} \left[\left(\mu + \mu_T \right) \left(\frac{\partial \bar{u}_i^n}{\partial x_j} + \frac{\partial \bar{u}_i^{n+1}}{\partial x_j} \right) \right] - \frac{\partial \bar{P}^{n+1}}{\partial x_i} \quad [A1]$$

where H_i is given by

$$H_i = - \frac{\partial}{\partial x_j} \left(\bar{u}_i \bar{u}_j \right) + \frac{\partial}{\partial x_j} \left(\frac{\mu_T}{\rho_0} \frac{\partial \bar{u}_j}{\partial x_i} \right) \quad [A2]$$

In the fractional-step method, an intermediate velocity field $(\tilde{\bar{u}}_i)$ is calculated by neglecting the pressure-gradient term in the momentum equations.

$$\frac{\tilde{\bar{u}}_i - \bar{u}_i^n}{\Delta t} = \frac{3}{2} H_i^n - \frac{1}{2} H_i^{n-1} + \frac{1}{2\rho_0} \frac{\partial}{\partial x_j} \left[\left(\mu + \mu_T \right) \left(\frac{\partial \bar{u}_i^n}{\partial x_j} + \frac{\partial \tilde{\bar{u}}_i}{\partial x_j} \right) \right] \quad [A3]$$

Then in the next step, the $(\tilde{\bar{u}}_i)$ field is corrected to satisfy continuity by solving for the pressure field. Subtracting Eq. [16] from [14] gives the following expression:

$$\frac{\bar{u}_i^{n+1} - \tilde{\bar{u}}_i}{\Delta t} = \frac{1}{2\rho_0} \frac{\partial}{\partial x_j} \left[\left(\mu + \mu_T \right) \frac{\partial (\bar{u}_i^{n+1} - \tilde{\bar{u}}_i)}{\partial x_j} \right] - \frac{\partial \bar{P}^{n+1}}{\partial x_i} \quad [A4]$$

Expressing the right-hand side of the previous equation in terms of the gradient of a scalar value (Φ) gives

$$\frac{\bar{u}_i^{n+1} - \tilde{\bar{u}}_i}{\Delta t} = - \frac{\partial \Phi^{n+1}}{\partial x_i} \quad [A5]$$

A Poisson equation can be obtained by applying the divergence operator to the previous equation:

$$\frac{\partial}{\partial x_i}\left(\frac{\partial \Phi^{n+1}}{x_i}\right) = \frac{1}{\Delta t}\left(\frac{\partial \bar{\tilde{u}}_i}{\partial x_i} - \frac{\partial \bar{u}_i^{n+1}}{\partial x_i}\right) = \frac{1}{\Delta t}\frac{\partial \bar{\tilde{u}}_i}{\partial x_i} \quad [A6]$$

Notice that the velocity field should satisfy the continuity equation, so the term containing the final corrected velocity divergence vanishes in the previous equation. The pressure and the scalar are related by

$$\bar{P}^{n+1} = \Phi^{n+1} - \frac{\Delta t}{2\rho_0}\left(\mu + \mu_T\right)\frac{\partial}{\partial x_i}\left(\frac{\partial \Phi^{n+1}}{x_i}\right) \quad [A7]$$

REFERENCES

1. B.G. Thomas, X. Huang, and R.C. Sussman: *Metall. Trans. B*, 1994, vol. 25B, pp. 527-47.
2. B.G. Thomas and L. Zhang: *Iron Steel Inst. Jpn. Int.*, 2001, vol. 41 (10), pp. 1181-93.
3. B.G. Thomas, L.J. Mika, and F.M. Najjar: *Metall. Trans. B*, 1990, vol. 21B, pp. 387-400.
4. D. Creech: *Mechanical and Industrial Engineering*, University of Illinois at Urbana–Champaign, Urbana, IL, 1999.
5. B.G. Thomas: in *Making, Shaping and Treating of Steel: Continuous Casting*, A. Cramb, ed., AISE Steel Foundation, Pittsburgh, PA, 2003, pp. 14.1-14.41.
6. C. Offerman: *Scand. J. Metall.*, 1981, vol. 10, pp. 25-28.
7. P.H. Dauby, M.B. Assar, and G.D. Lawson: *La Rev. Metall.–CIT*, 2001, vol. 98 (4), pp. 353-66.
8. B.G. Thomas, Q. Yuan, S. Sivaramakrishnan, T. Shi, S.P. Vanka, and M.B. Assar: *Iron Steel Inst. Jpn. Int.*, 2001, vol. 41 (10), pp. 1266-76.
9. D. Gupta, S. Chakraborty, and A.K. Lahiri: *Iron Steel Inst. Jpn. Int.*, 1997, vol. 37 (7), pp. 654-58.
10. D. Gupta and A.K. Lahiri: *Metall. Mater. Trans. B*, 1994, vol. 25B, pp. 227-33.
11. D. Gupta and A.K. Lahiri: *Metall. Mater. Trans. B*, 1996, vol. 27B, pp. 757-64.
12. R. Sobolewski and D.J. Hurtuk: *2nd Process Technology Conf. Proc.*, ISS, Warrendale, PA, 1982, pp. 160-65.
13. X. Huang, B.G. Thomas, and F.M. Najjar: *Metall. Trans. B*, 1992, vol. 23B, pp. 339-56.
14. B.G. Thomas and F.M. Najjar: *Appl. Mathematical Modeling*, 1991, vol. 15 (5), pp. 226-43.
15. S.H. Seyedein and M. Hasan: *Int. J. Heat Mass Transfer*, 1997, vol. 40 (18), pp. 4405-23.
16. S.H. Seyedein and M. Hasan: *Can. Metall. Q.*, 1998, vol. 37 (3–4), pp. 213-28.
17. CFX 4.2., AEA Technology, Pittsburgh, PA, 1998.
18. B.G. Thomas, R. O'Malley, T. Shi, Y. Meng, D. Creech, and D. Stone: *Modeling of Casting, Welding, and Advanced Solidification Processes*, Shaker Verlag GmbH, Aachen, Germany, 2000, pp. 769-76.
19. B.G. Thomas, R.J. O'Malley, and D.T. Stone: *Modeling of Casting, Welding, and Advanced Solidification Processes*, TMS, Warrendale, PA, 1988, pp. 1185-99.
20. J. Tannehill, D. Anderson, and R. Pletcher: *Computational Fluid Mechanics and Heat Transfer*, 2nd ed., Taylor and Francis, Washington, DC, 1997.
21. Q. Yuan, S. Sivaramakrishnan, S.P. Vanka, and B.G. Thomas: *Metall. Mater. Trans. B*, 2004, vol. 35B, pp. 967-82.
22. Q. Yuan, B.G. Thomas, and S.P. Vanka: *Metall. Mater. Trans. B*, 2004, vol. 35B, pp. 685-702.
23. Q. Yuan, B.G. Thomas, and S.P. Vanka: *Metall. Mater. Trans. B*, 2004, vol. 35B, pp. 703-14.
24. T. Shi: *Materials Science and Engineering*, University of Illinois at Urbana–Champaign, Urbana, IL, 2001.
25. J. Boussinesq: *Theorie Analytique de la Chaleur*, Gauthier–Villars, Paris, 1903, vol. 2.
26. K. Horiuti: *J. Phys. Soc. Jpn.*, 1985, vol. 54 (8), pp. 2855-65.
27. B. Zhao, S.P. Vanka, and B.G. Thomas: *Int. J. Heat Fluid Flow*, 2005, vol. 26, pp. 105-18.
28. I. Jimbo and A. Cramb: *Metall. Trans. B*, 1993, vol. 24B, pp. 5-10.
29. B. Zhao: *Mechanical and Industrial Engineering*, University of Illinois at Urbana–Champaign, Urbana, IL, 2003.
30. H. Bai and B.G. Thomas: *Metall. Mater. Trans. B*, 2001. vol. 32B, pp. 253-67.
31. H. Bai and B.G. Thomas: *Metall. Mater. Trans. B*, 2001, vol. 32B, pp. 269-84.
32. F.M. Najjar, B.G. Thomas, and D.E. Hershey: *Metall. Trans. B*, 1995, vol. 26B, pp. 749-65.
33. G.D. Lawson, S.C. Sander, W.H. Emling, A. Moitra, and B.G. Thomas: *Steelmaking Conf. Proc.*, ISS, Warrendale, PA, 1994, pp. 329-36.
34. C. Li and B.G. Thomas: *Brimacombe Memorial Symp.*, CIM, Montreal, 2000, pp. 595-611.
35. R.J. Goldstein and M.E. Franchett: *J. Heat Transfer*, 1988, vol. 110, pp. 84-90.
36. Q. Yuan, B. Zhao, S.P. Vanka, and B.G. Thomas: *Steel Res. Int.*, 2005, vol. 76 (1), pp. 33-43.